Hydrothermally grown Pb^{2+} doped ZnO nanorods for hydrogen and acetylene gas sensing

By

Sipho Tumi Ngqondo

Dissertation presented in partial fulfilment of the requirements for the degree of

Master of Science

to the

DEPARTMENT OF PHYSICS
UNIVERSITY OF ZULULAND

Supervisor: Prof. O.M. Ndwandwe

Department of Physics, University of Zululand

27 APRIL 2008

DECLARATION

I, the undersigned, hereby declare that the work contained in this dissertation is my own original work and that I have not previously in its entirety or in part submitted it at any university for a degree.

Signature :……

Date :……/……/……..

To my family…….

…….……with Love

Acknowledgements

It is with a feeling of sincere gratitude that I acknowledge the financial assistance which I received from the NRF and the Research Committee of the University of Zululand. I would also like to use this opportunity to express my gratitude to:

- Prof. OM Ndwandwe, Head of Physics Department, University of Zululand, for his guidance and informative discussions throughout his supervision of this work.

- Dr C. Theron, Former Head, Materials Research Group, iThemba Labs Cape Town, for making the facilities at MRG available for some of the experiments.

- Dr. O. Nemroui, Associate Professor, University of Zululand, for help with some of the experiments.

- Dr M. Maaza, Nanosciences group, iThemba Labs for helping me on hydrothermal synthesis techniques.

- Dr L. Vayssierres, Japan young Scientist, for his assistance on hydrothermal synthesis techniques.

- Dr Forbes, CSIR, National Laser Centre, for making the facilities available for my research.

- P.S. Sibiya, CSIR, Candidate Researcher, for his friendship and assistance with the PLD.

- PS Mkwae, for his jokes, encouragements, friendship and other things.

- V. Msomi, for friendship, encouragements and cover-ups.

- C.L. Ndlangamandla, for making an eye opening suggestion, which proved to be very useful for this work.

- My mother, father and my brother S'bu for their moral support and understanding.

- A Special dedication to all those who contributed, but not mentioned, the list had a potential of being infinitely long BAFETHU!!!!!!!!! Ngeke nginibale nonke noma sengithanda, nizongena kuluzayo uhla nina.

"JIBA……ONGADLIWA……NYONI."

ABSTRACT

Randomly orientated ZnO nanorods were deposited hydrothermally on Si <100> wafers. The precursor solutions used for ZnO nanorods deposition were zinc chloride + aqueous ammonia and Zinc nitrate + HMT. ZnO nanorods were deposited on Si<100> wafers to establish the optimal PH and concentration which yield the best substrate coverage for each precursor solution. ZnO thin films were deposited on glass substrates using pulsed laser deposition. These thin films were used for both gas sensing and as seed for orientated ZnO nanorods deposition. Rutherford Backscattering was used to measure the thickness and stochiometry of the deposited ZnO films. Orientated ZnO nanorods were then deposited on glass slides with ZnO thin films using the optimal PH and concentration for reagents established when Si<100> wafers were used as substrates. Pb doped ZnO nanorods were prepared by adding Lead (II) Nitrate as the Lead source into Zinc nitrate + HMT precursor solution. These Pb doped ZnO nanorods were then deposited on glass substrates with a ZnO thin film. The crystal structure and preferred plane orientation of all samples was studied using X-ray diffraction. Morphological and elemental analysis of samples was investigated using Scanning Electron Microscopy equipped with EDX. All samples showed good ZnO stochiometry with no foreign atoms except the samples with Pd doped ZnO nanorods. Ag contacts were deposited on the samples using EDWARDS vacuum coater. The gas sensing characteristics were investigated on all samples using 20% hydrogen and acetylene as test gases while 80% nitrogen was used as a carrier gas. ZnO thin films were found be at optimum for hydrogen gas sensing in the range 300-350^{o}C, the minimum temperature for acetylene sensing was 400^{o}C. Orientated ZnO nanorods also operated at their optimum in the 300-350^{o}C range like thin-films, however they exhibited better sensitivity in this range than thin films. ZnO nanorods started sensing acetylene at 350^{o}C, slightly lower than ZnO thin films. Pb doped ZnO nanorods were able to sense hydrogen with 67% sensitivity at 250^{o}C. These Pb doped ZnO nanorods were also found to be cable of sensing acetylene in the whole temperature range.

CONTENTS

LIST OF FIGURES

LIST OF TABLES

CHAPTER 1

1. BACKGROUND AND SCOPE OF INVESTIGATION

1.1. Structural properties of Zinc Oxide

Zinc oxide (ZnO) is a well-known wide band gap semiconductor (3.37 eV at room temperature) **[30]**, which has a wurtzite structure with a lattice parameter a = 0.325 nm and c=0.512 nm. The distance between Zn^{2+} ion and O^{2-} ion along the c-axis is 0.1992 nm, and the distance between these two ions along other three axes is 0.1973 nm. The two major characteristics of the ZnO structure are the non-central symmetry and polar surfaces. The structure of ZnO can be described as a number of alternating planes composed of tetrahedrally coordinated O^{2-} and Zn^{2+} ions, which are stacked alternately along the c-axis **[15].**

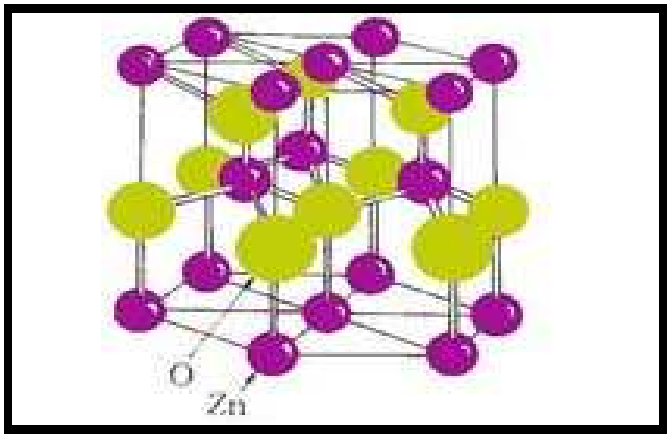

Figure 1.1**: The hexagonal structure of ZnO showing the arrangement of Zn^{2+} and O^{2-} atoms **[15]

The oppositely charged ions produce positively charged $–Zn^{2+}$ and negatively charged $–O^{2-}$ polar planes, which result in a normal dipole moment and spontaneous polarization along the c-axis and different surface energy with the different crystallographic orientations. ZnO thin films generally exhibit a good optical transmission (over 80%) in the visible and near infrared wavelength range due to its wide bandgap energy. This transmission value of ZnO thin films depends on its microstructure and roughness. The optical band gap of ZnO can shift by the introduction of intrinsic or extrinsic dopants. This shift is called the Burstein-Moss effect. As the carrier concentration increases, the Fermi energy moves above the conduction band edge, which results from the complete occupation of states at the bottom of the conduction band. Therefore, optically stimulated transitions from valence band to these states can not occur, and the optical band gap of ZnO increases **[15].**

In order to enhance the electrical conductivity in ZnO, the goals are to increase the carrier concentration and mobility simultaneously. However, it is difficult to increase these two values simultaneously because these two values are interrelated with each other. The increase of carrier concentration can be achieved in two ways. The first way is creating intrinsic dopants through lattice defects such as oxygen vacancies or zinc interstitials. The second way is the introduction of extrinsic dopants such as trivalent atoms at zinc lattice sites and halogen atoms at oxygen lattice sites. The mobility of carrier depends on the microstructure such as grain boundary and other defects. Smaller grain sizes induce a higher probability that an electron will encounter a scattering event resulting in a decrease in mobility **[15].**

1.2 Nanosized ZnO Particles

As a result of the high surface area to volume ratio of ZnO nanostructures, the nature of the surface is very important when considering the properties of nanosized ZnO particles. There have been reports of many methods for synthesizing ZnO nanosized particles **[2]**.

1.3 ZnO Nanorods

Growing interest in one-dimensional (1-D) oxide materials, especially ZnO nanorods, is being displayed due to their novel properties and potential applications. ZnO nanorods have been synthesized by various methods such as the chemical vapour transport and condensation process, template-based growth method, and wet chemical synthesis **[2]**.

1.4 Synthesis of ZnO Nanostructures

The general deposition of metal oxides onto substrates and fabrication of coatings such as dense thin films to micro-particulate thin films have been mastered for several decades and the plethora of physical and chemical processing techniques is available **[2]**. The techniques such as molecular beam epitaxy (MBE), oxygen plasma assisted MBE, ion beam assisted deposition (IBAD), Electron beam evaporation, laser-assisted catalytic growth, laser pyrolysis , pulsed laser deposition, thermal evaporation, metal organic vapour phase epitaxy, vapour liquid solid catalytic growth, spray pyrolysis, chemical vapour deposition, radio frequency magnetron sputtering, liquid phase deposition, spin coating, dip coating, electro-deposition, electrostatic self-assembly and Langmuir-Blodgett techniques are the most utilized by the Scientists and Engineers.

1.4.1 Wet Chemical Methods

Solution chemistry based and wet chemical techniques represent the most economical and simplest technique to produce 3-D arrays on a large scale. They will contribute significantly to the manufacturing of raw nanostructures and play a large part in the fabrication of practical nanodevices. Such methods are template based synthesis, electro deposition techniques, and aqueous chemical growth **[2]**.

1.4.1.1 Aqueous Chemical growth

This novel technique has emerged recently as a simple and powerful tool to fabricate, at low cost and mild temperatures **[2]**, large areas of metal oxide nano to microparticulate thin films. 3D arrays consisting of orientated anisotropic nanoparticles are easily generated with enhanced control over the orientation and the dimensions. The synthesis involves the controlled heteronucleation of metal oxides in aqueous solutions. The most pertinent parameter to control is the nucleation and therefore the overall design and architecture of a thin film is dependent on the interfacial free energy of the system.

The main idea here is to play on the thermodynamics and the kinetics of nucleation, growth, and ageing of the systems controlling experimentally their interfacial tension. The ability to segregate the nucleation and the growth stage enables control of the monodisperity of the system. Indeed performing the aqueous precipitation far from the typical point of zero charge (PZC) of the metal oxide allows enhanced control of the nucleation, growth, and the ageing process.

According to the well-known acid-base surface properties of metal oxides, decreasing (or increasing) the PH of precipitation from the PZC will increase the surface charge density by adsorption of protons (or hydroxyl ions) and consequently reduce interfacial tension of the system. In addition, a high ionic strength will also increase the surface charge density by screening the electrostatic repulsion at the interface, and allowing more surface site to develop a charge.

The surface charge may therefore reach its maximum, which is directly related to the composition and the structure of the surface oxygen. This will contribute to a further lowering of the interfacial tension of the system. From then on, thermodynamic, colloidal stability may thus be reached, resulting in a considerable lowering of the secondary ageing process and hence-forth maintaining constant size and shape of the nanoparticles as well as avoiding crystal phase (and morphological) transformations.

By careful consideration of the parameters involved in the nucleation and growth processes, the free enthalpy of nucleation shows a maximum as a function of the particle size, which depends on the interfacial tension at the cubic power. Therefore, reducing the interfacial tension leads to an important lowering of the nucleation energy barrier, leading to the reduction of the particle size and its distribution.

The experimental verification on the aqueous precipitation of spinel iron oxide (i.e., magnetite Fe_3O_4) at room temperature has clearly illustrated that the thermodynamic stability of metal oxide nanoparticles does exist. It also demonstrated that the average particle size may experimentally be monitored and empirically predicted over an order of magnitude in the nanometre range with narrow size distribution.

The excellent agreement between theory and experiments has yielded strong evidence for efficient growth control of metal oxide nanoparticles under low interfacial tension conditions; it has also produced great expectation for the future development of nano-materials devices and the optimization of their physical properties. Moreover, when the thermodynamic stabilization is achieved, not only is the size tailored but also the shape as well as crystallographic structure maybe controlled. For instance at low interfacial tension, the particle shape does not need to be spherical; indeed, very often nanoparticles are spherical to minimize the surface energy because the sphere represents the smallest surface for a given volume. However, if the synthesis or dispersion condition is suitable (i.e., yielding to the thermodynamic stabilization of the system), the shape of the crystallites will be driven by the symmetry of the crystal structure and an anisotropy may therefore be developed. Manipulating and controlling the interfacial tension enables one to grow nanoparticles with various sizes and shapes.

Applying the appropriate solution chemistry (precipitation and dispersion media) to transition metal ions along with the natural crystal symmetry and anisotropy or forcing the material to

grow along a certain crystal direction by controlling chemically the thermodynamics and kinetics of nucleation, growth, and ageing phenomena, one can reach the ability to develop novel crystal morphologies. In addition to particle size and shape control, precipitating nanoparticles at “zero” interfacial tension allows stabilization of metastable crystal phases.

Crystal phase transition in a solution usually operates through a dissolution-re-crystallization process to minimize the surface energy of the system. Indeed, when a solid offers several allotropic phases it is generally the one with the highest solubility and consequently the lowest stability (i.e., the crystallographic metastable phase that precipitate first). This is understood by considering the nucleation kinetics of the solid. At a given super-saturation ratio, the germ size is as small and the nucleation speed as fast as the interfacial tension of the system is low.

Thus, because the solubility of is inversely proportional to interfacial tension, the precipitation of the most soluble phases and consequently the thermodynamically less stable phases are the therefore kinetically promoted. Indeed, due to its solubility and metastability, this particular phase is more sensitive to secondary growth and the ageing that lead to crystallographically more stable phases essentially by heteronucleation.

1.4.2 Hydrothermal synthesis

Hydrothermal synthesis includes various techniques of crystallizing substances from high-temperature aqueous solutions at high vapour pressures; also termed "hydrothermal method"**[24]**.

The term "hydrothermal" is of geologic origin. Geochemists and mineralogists have studied hydrothermal phase equilibria since the turn of the century. George W. Morey at the Carnegie Institution and later, Percy W. Bridgman at Harvard University did much of the work to lay the foundations necessary to containment of reactive media in the temperature and pressure range where most of the hydrothermal work is conducted.

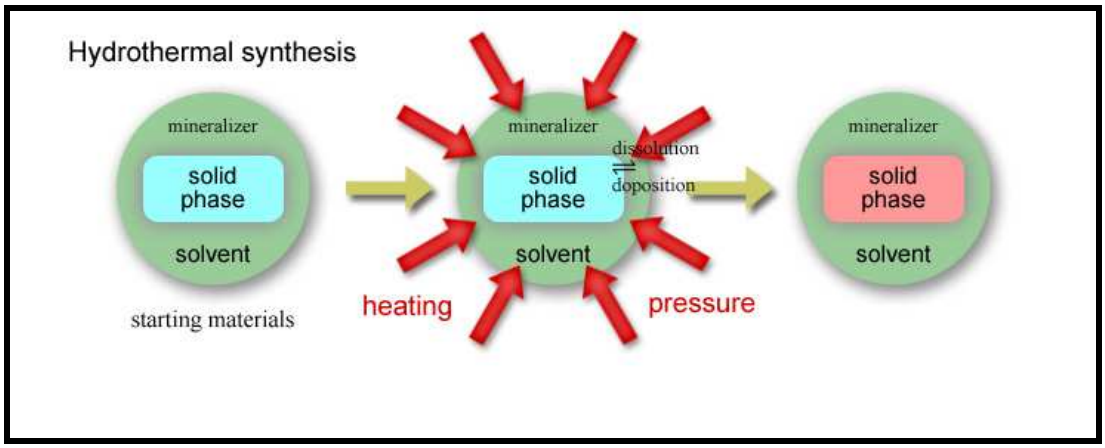

Figure 1.2**: The process of hydrothermal synthesis, reviling the importance of pressure and heat for the process occur at an optimal rate **[29]

Hydrothermal synthesis can be defined as a method of synthesis of single crystals which depends on the solubility of minerals in hot water under high-pressure see **Figure 1.2**. The crystal growth is performed in an apparatus consisting of a steel pressure vessel called autoclave, in which a nutrient is supplied along with water. A gradient of temperature is maintained at the opposite ends of the growth chamber so that the hotter end dissolves the nutrient and the cooler end causes seeds to take additional growth.

The super saturation is the most extensively used method in hydrothermal synthesis and crystal growing. The super-saturation is achieved by reducing the temperature in the crystal growth zone **[23]**. The nutrient is placed in the lower part of the autoclave filled with a specific amount of solvent. The autoclave is heated in order to create two temperature zones. The nutrient dissolves in the hotter zone and the saturated aqueous solution in the lower part is transported to the upper part by convective motion of the solution. The cooler and denser solution in the upper part of the autoclave descends while the counter flow of solution ascends. The solution becomes supersaturated in the upper part as the result of the reduction in temperature and crystallization sets in.

1.5 Advantages of aqueous chemical growth

The aqueous chemical growth method consists of heating an aqueous solution of metal salts or complexes in the presence of a substrate at moderated temperatures (below 100 ^{o}C) in a closed vessel **[25]**. Therefore, such technique does not require high-pressure containers and is also entirely recyclable, safe and environment friendly because only water is used as a solvent. Such a process avoids the safety hazards or organic solvents and their eventual evaporation and potential toxicity. In addition because no organic solvents or surfactants are present, the purity of the materials is substantially improved.

The residual salts are easily washed out by water due to their high solubility. In most cases no additional heat or chemical treatment is necessary, which represents a significant improvement compared with surfactant-, template-, or membrane based synthesis methods.

Full coverage of the substrate is obtained within a few hours provided that the heat capacity of water and surface coverage control are achieved by monitoring the synthesis time in the early stages of the thin film growth. Partial coverage is obtained within the first hours, which maybe necessary for certain application to adjust and tune the overall physical properties of the devices (e.g., optical properties of multi-band gap thin films).

1.6 Metal oxide Gas Sensors

Conductometric gas sensors based on semiconducting metal oxides are actually one of the most investigated groups of gas sensors **[20]**. They have attracted the attention of many users and scientists interested in gas sensing under atmospheric conditions due to the: low cost and flexibility associated to their production; simplicity of their use; large number of detectable gases/possible application fields. Their applications span from “simple” explosive or toxic gases alarms (see information provided by the gas sensors manufacturers on their homepages) to air intake control in cars to components in complex chemical sensor systems.

On the side of R&D work the most visible result is a large number of publications, generally reporting excellent individual gas sensing performance. The latter is obtained mainly by measuring the signals of laboratory samples (change of sample/sensor’s electrical resistance) in quite unrealistic environments from the viewpoint of real sensors’ working conditions, i.e. in the absence of carrier gases like nitrogen/Oxygen.

The performance of a sensor is very much dependent on the sensors fabrication technologies (type of substrate and electrodes, thickness and morphology of the sensing layer, etc.), which indicates that the spectroscopic input should also be gained on actual sensors and not on sensing material samples.

1.7 The Metal Oxide Gas Sensor Design approach

The final objective of R&D activities is the design and fabrication of good gas sensors well suited for solving a certain application problem. It is important to keep in mind that the quality of a sensor is almost impossible to be defined without understanding the application needs, which besides the target gas/gases **[20]**, possible cross-interferences and environmental conditions also relate to the cost/price restrictions of the instrument using the sensors. The latter factor is generally described as the fourth S – suitability – that is more and more considered in addition to the three classical ones (sensitivity, selectivity, stability). In order to understand the challenges of the research in the field, one should have a look at the way in which the sensor signal is generated. A sensor element normally comprises the following parts:

- **Sensitive layer** deposited over a
- **Substrate** provided with
- **Electrodes** for the measurement of the electrical characteristics.

The device is generally heated by its own

- **Heater;** this one is separated from the sensing layer and the
- **Electrodes** by an electrical insulating layer.

Such a device is normally operated in air, in the presence of humidity and residual gases (e.g. carbon dioxide). It is generally accepted that in such conditions, at working temperatures between 200 and 400 ◦C, at the surface of the sensitive material – the metal oxide – various oxygen, water and carbon dioxide-related species are present. Not all of them have a direct influence on the sensor resistance id est. are involved in free charge carrier exchanges with the metal oxide (ionosorption); for a general discussion on the different types of adsorptions. Some species will form bonds by exchanging electrical charge with specific surface sites (surface atoms), meaning that they may form dipoles; the latter will not affect the concentration of free charge carriers so that they will not have an impact on the resistance of the sensitive layer.

Those situations are described in **Figure 1.3** for the simplified case of adsorbed oxygen ions, as electron traps, and hydroxyl groups bound to the metal, as dipoles, at the surface of a n-type metal oxide semiconductor; expressed in the energy bands formalism for the metal oxide, the effect of the former is a band bending while the effect of the latter is a change of the electronic affinity when compared to the situation existing before the adsorption took place.

Changes in the band bending, induced by, e.g. by the reaction of the oxygen ions with carbon monoxide, will be translated into changes of the overall electrical resistance/conductance of the sensitive layer. It looks simple but it is not and the simple proof is the well-known influence of the ambient humidity on the sensor signal upon CO exposure; this indicates that the reaction cannot be that simple and there should be some involvement of species that do not have an obvious, measurable electrical resistance effect.

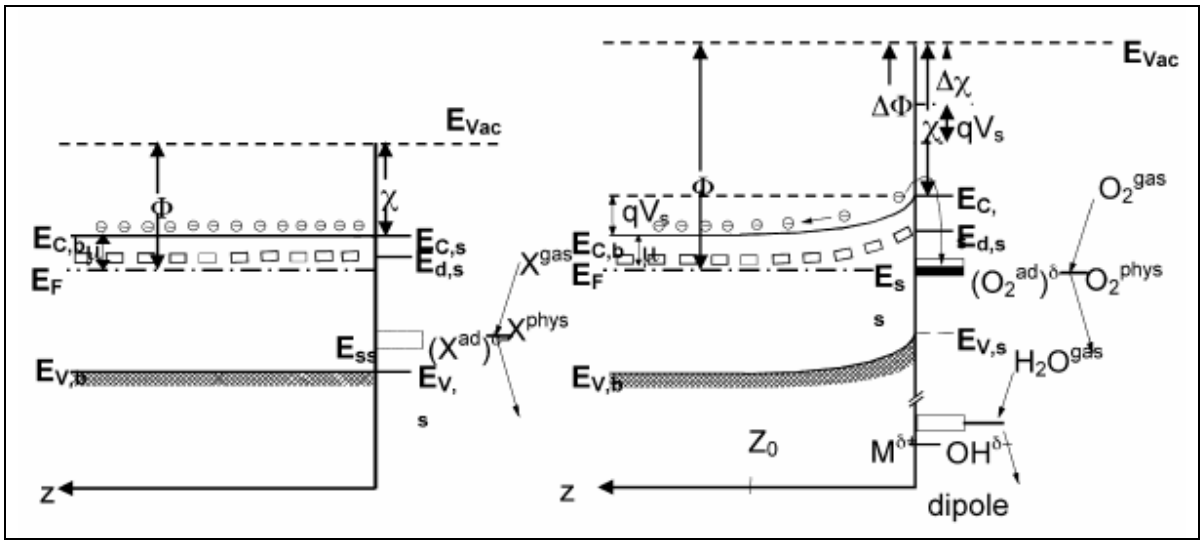

Figure 1.3*: Schematic representation of (left) flat band in n-type semiconductor and (right) band banding model illustrating adsorption at the surface of n-type semiconductor. The changes of the work function (Δ Φ) are determined by band bending (qVs—due to ionosorption) and changes the electron affinity (Δ χ) due to building of dipoles at the surface (Mδ+–OHδ−).**[20]***

1.8 Contacts used for ZnO

1.8.1 n-Type ohmic contacts

The achievement of acceptable ZnO device characteristics relies heavily on developing low specific contact resistance ohmic metallization schemes. The usual approaches involve surface cleaning to reduce barrier height or increase of the effective carrier concentration of the surface through preferential loss of oxygen. Specific contact resistances of ~ 3 x 10^{-4} Ω.cm^{-3} were reported for Pt–Ga contacts on n-ZnO epitaxial layers, 2 x 10^{-4} Ω.cm^{-3} for Ti/Au on Al-doped epitaxial layers , 0.7 Ωcm^{-3} for non-alloyed In on laser processed n-ZnO substrates , 2.5 x 10^{-5} Ω.cm^{-3} for non-alloyed Al on epitaxial n-type ZnO , 7.3 x 10^{-3} to 4.3 x 10^{-5} Ω.cm^{-3} for Ti/Au on

plasma exposed, Al-doped n-type epitaxial ZnO and 9 x 10^{-7} Ω.cm^{-3} for Ti/Al on n+-epitaxial ZnO **[22]**. Several points are clear from the past works, namely that the minimum contact resistance generally occurs for post-deposition annealing temperatures of 200–300 ^{o}C on doped samples which must be treated so as to further increase the near-surface carrier concentration

Table 1: *Presents the resistivity of contacts which are normally used for ZnO for both p and n type.* ***[22].***

Ohmic contacts ZnO and their respective specific contact resistance from published works

Description	Metal	Lowest ρ_c (Ωcm^2)
(a) *n-type*		
n-ZnO epi on Al_2O_3	Ti/Au	1.5×10^{-5}
n-ZnO epi on Al_2O_3	FIB direct write Ga–Pt	3.1×10^{-4}
n-ZnO epi on Al_2O_3	E-beam Ti/Au	2×10^{-4}
n-ZnO epi on Al_2O_3	E-beam Ti/Au	4.3×10^{-5}
n-ZnO epi on Al_2O_3	E-beam Re/Ti/Au	1.7×10^{-7}
n-ZnO epi on Al_2O_3	E-beam Ti/Al	9.0×10^{-7}
n-ZnO epi on Al_2O_3	E-beam Al/Pt	2×10^{-6}
n-ZnO epi on Al_2O_3	E-beam Ru	2.1×10^{-5}
n-ZnO epi on Al_2O_3	E-beam Al	8×10^{-4}
n-ZnO bulk	E-beam Ti/Au	5×10^{-5}
n-ZnO bulk	E-beam In	7×10^{-1}
(b) *p-type*		
p-ZnO epi on Al_2O_3	E-beam Ti/Au	1.72×10^{-4}
p-ZnO epi on Al_2O_3	E-beam Pt/ITO	7.7×10^{-4}
p-ZnMgO epi on glass	E-beam Ti/Au or Ni/Au	3×10^{-3}
p-ZnMgO epi on glass	E-beam Ni/Au	4×10^{-5}
p-ZnO on SiC	E-beam In/Au, Ti/Au, or Ni/Au	—

1.8.2 p-Type ohmic contacts

In addition to achieving stable and high hole concentrations, work is also needed to develop low-resistance p- ohmic contacts. Previous reports have shown that Au, Ni, Pt and Ni/Au metallurgy can be used as ohmic metallization on thin films of p-type ZnO or ZnMgO. A specific contact resistance of 1.7 x 10^{-4} Ω.cm^2 was reported after annealing at 600 ^{o}C in air was achieved for Ni/Au on P-doped ZnO produced by sputtering. Both Au and Au/Ni/Au are found to provide low

specific contact resistance on lightly doped p-ZnMgO after annealing at 600 ^{o}C **[22]**. In both cases, the as-deposited contacts are rectifying and the transition to ohmic behaviour is associated with out-diffusion of Zn from the ZnMgO, as shown in **Figure 1.4**. A minimum specific contact resistance of 7.6 x 10^{-6} $\Omega.cm^2$ was obtained with Au/Ni/Au, which is about a factor of 3 lower than for pure Au contacts annealed at the same temperature. **Table 1** shows a summary of reported p-ohmic contacts on ZnO. Ohmic and Schottky contacts to p-type $Zn_{0.9}$ $Mg_{0.1}O$ have recently been studied in our lab, on material that is P doped during pulsed laser deposition and subsequently annealed to reduce the background n-type conduction **[22].**

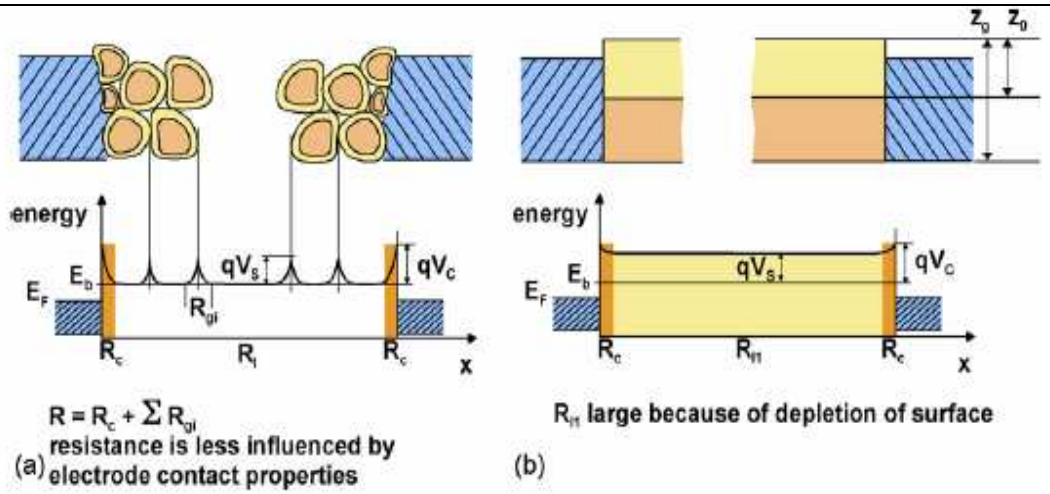

Figure 1.4: *Schematic representation of a porous (a) and a compact (b) sensing layer with energy bands. Represents the effects of contact properties and the type of electrode on resistance properties* ***[20]****.*

1.9 Zinc Oxide gas sensors

Generally a large number of repetitive steps of nanorod-based sensors are involved in metal oxide nanorods such as ZnO, MoO_3, and tungsten oxide nano-sensors, polymer nanorods such as poly(3,4-ethylene-dioxythiophene) nanosensor, and metal nanorods such as Au nanosensor. Among these researches, most attention has been focused on ZnO nanorods sensors. Wang and co-workers **[3, 4]** fabricated thick film sensors based on ZnO nanorods. The paste prepared from a mixture of ZnO nanorods with a polyvinyl alcohol solution was coated onto an Al_2O_3 tube on which two gold leads had been installed at each end. A heater of Ni Cr wire was inserted into the Al_2O_3 tube to supply the operating temperature which was controlled in the range of 100–500 ◦C.

The ZnO nanorod sensors could detect 1 ppm C_2H_5OH (350 ◦C) and 0.05 ppm H_2S (25 ◦C). It was suggested that the gas response was mainly dependent upon two factors. The first is the amount of active sites for oxygen and the reducing gases on the surface of the sensor materials. The more active sites the surface of nanosensor contain, the higher sensitivity the sensor exhibits. The second is the reactivity of the reducing gases.

The bond energy of H-SH in H_2S is 381 kJ/mol **[5]**, so that it is easy to open the bond H-SH at lower temperature. On the other hand, the bond energies H-CH_2, H -OC_2H_5 and H CH in C_2H_5OH are 473, 436 and 452 kJ/mol, respectively, so that it is difficult to open the bonds in C_2H_5OH at lower temperature.

Wang and co-workers presented the sensitivity to 10 ppm H_2 and 1000 ppm C_2H_5OH of Pd/multiple **[8]** and multipod-shaped **[9]** ZnO nanorods sensors. The dominant mechanism for this sensing process is more likely to be the chemisorption of hydrogen on the Pd surface. Multipod ZnO nanorods which have more than four even tens of needle-like nanorods at a common **[10]** junction resulted in a very large surface area, and therefore their sensing properties related to the surface reactions could be greatly enhanced.

Xu et al. **[11, 12]** found the treatment process of ZnO nanorods had obvious effect on its gas sensing properties to HCHO, LPG, and H_2S. Zhang et al. **[13]** reported ZnO nanorods for a reagentless uric acid biosensor. The uricase/ZnO biosensor was constructed by casting uricase on the ZnO membrane. The electrocatalytic response showed a linear dependence on the uric acid concentration ranging from 5.0×10^{-6} to 1.0×10^{-3} M with a detection limit of 2 M. In their work, ZnO nanorods played the role of an efficient electron-conducting tunnel and had a very high specific surface area. Consequently, the uricase attached to the ZnO nanorods surface had more spatial freedom in its orientation, which facilitated the direct electron transfer between the active sites of the immobilized uricase and the electrode surface.

1.10 Scope of Investigation

In this study, synthesis, characterization and gas sensing properties of ZnO thin films, orientated ZnO nanorods and ZnO nanorods doped with Pb are presented. The gas sensing properties of all samples were investigated in the temperature range between 100-400 ^{o}C. The test gases used for this study were hydrogen and acetylene. The concentration of both test gases used remained

constant at 20 vol% in nitrogen for all experiments. Chapter 1 presents an overview of the literature survey of related subjects to this research. Chapter 2 presents the experimental, sample preparation methods and characterization techniques. Chapter 3 presents the methods used to design the gas testing chamber used for this study. Chapter 4 presents the results and discussions of ZnO thin films deposited on glass substrates using PLD and their gas sensing characteristics.

Chapter 5 presents the results and discussions of ZnO nanorods deposited on bare Si<100> wafers. The deposition of ZnO nanorods on bare silicon wafers was performed to obtain optimum concentration and PH values for the precursor solutions used which gave the best substrate coverage. The obtained optimum concentration and PH values are the values used to prepare orientated ZnO nanorods, doped and un-doped. Chapter 6 presents the results and discussions of data obtained from vertically orientated ZnO nanorods deposited on substrates with ZnO thin-films (ZnO seeds). In this chapter these nanorods are characterised and tested for gas sensitivity. Chapter 7 presents the results and discussions of vertically orientated Pd doped ZnO nanorods deposited on glass substrates with ZnO thin films. The dependence of sensitivity on the concentration of the doping element is not investigated. The research focused on a single concentration of Pb which is ten times less than that of precursor reagents. Chapter 8 is the summary and conclusions of this work.

CHAPTER 2

2. EXPERIMENTAL PROCEDURES

2.1 Sample preparation

2.1.1 Preparation and cleaning of substrates

Microscope glass slides were purchased from Industrial analytical (PTY) LTD. These glass slides were then cut into small square pieces with an area of 100 mm^2. This area was chosen to ensure a good XRD signal from the exposed area and enough space for the deposition of Ag contacts. The as-cut glass pieces were chemically cleaned with methanol, trailed by acetone, then trichloroethylene, acetone, methanol and lastly deionised water. The stirring was carried out using an ultrasonic bath. After the cleaning procedure, the samples were then dried in air. These samples were then placed on a sample holder of the Pulsed-Laser deposition system one at a time using silver paint and used as substrates for ZnO thin film deposition.

2.2. Pulsed Laser Deposition

Pulsed laser deposition was used to deposit nanosized thin films of ZnO on glass substrates. Pulsed laser deposition (PLD) is a thin film deposition (specifically a physical vapour deposition, PVD) technique where a high power pulsed-laser beam is focused inside a vacuum chamber to strike a target of the desired composition **[27]**. The material is then vaporised from the target and deposited as a thin film on a substrate, such as a silicon wafer or glass facing the target.

While the basic-setup is simple relative to many other deposition techniques, the physical phenomena of laser-target interaction and ZnO thin film growth are quite complex. When a laser pulse is absorbed by the ZnO target; energy is first converted to electronic excitation and then into thermal, chemical and mechanical energy resulting in evaporation, ablation, plasma formation and even exfoliation. The ejected species expand into the surrounding vacuum in the form of a plume containing many energetic species including atoms, molecules, electrons, ions, clusters, particulates and molten globules, before depositing on the typically hot substrate.

The detailed mechanisms of PLD are very complex including the ablation process of the ZnO by the laser irradiation, the development of a plasma plume with high energetic ions, electrons as well as neutrals and the crystalline growth of the film itself on the heated substrate. The process of PLD can generally be divided into four stages:

- Laser ablation of the target material and creation of a plasma
- Dynamic of the plasma
- Deposition of the ablation material on the substrate
- Nucleation and growth of the film on the substrate surface

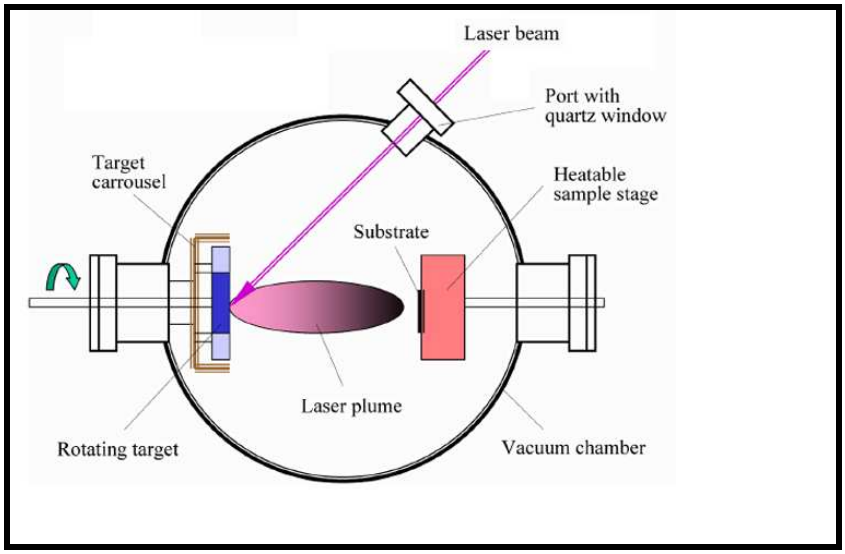

***Figure 2.1**: A schematic representation of how Pulsed laser deposition works **[28]**.*

Each of these steps is crucial for the crystallinity, uniformity and stoichiometry of the resulting ZnO thin film. The ablation of ZnO upon laser irradiation and the creation of plasma are very complex processes. The removal of atoms from the target is done by vaporization of the bulk at the surface region in a state of non-equilibrium and is caused by a Coulomb explosion. In this the incident laser pulse penetrates into the surface of the ZnO target within the penetration depth. This dimension is dependent on the laser wavelength and the index of refraction of the target material at the applied laser wavelength and is typically in the region of 10 nm for most materials. The strong electrical field generated by the laser light is sufficiently strong to remove the electrons from the ZnO target of the penetrated volume.

This process occurs within 10 ps of a ns laser pulse and is caused by non-linear processes such as multi-photon ionization which are enhanced by microscopic cracks at the surface, voids, and

nodules, which increase the electric field. The free electrons oscillate within the electromagnetic field of the laser light and can collide with the atoms of the bulk material thus transferring some of their energy to the lattice of the target material with in the surface region. The surface of the target is then heated up and the material is evaporated. The temperature of the generated plasma plume is typically 10000 K.

In the second stage the material expands in the plasma parallel to the normal vector of the target surface towards the substrate due to Coulomb repulsion and recoil from the target surface. The spatial distribution of the plume is dependent of the background pressure inside the PLD chamber. The density of the plume can be described by a $\cos^n(x)$, law with a shape similar to a Gaussian curve. The dependency of the plume shape on the pressure can be described in three stages: (1) the vacuum stage, where the plume is very narrow and forward directed; almost no scattering occurs with the background gases. (2) The intermediate region where the splitting of the high energetic ions from the less energetic species can be observed.

The as-deposited ZnO thin-films were used as seeds for hydrothermal synthesis of vertically orientated ZnO nanorods. Different characterization tools and techniques were used to analyze the structural and the morphological characteristics of ZnO thin-films deposited.

2.4. Sample characterization

2.4.1 Scanning Electron Microscopy (SEM)

2.4.1.1 SEM Sample preparation

The specimens examined by SEM must be able to withstand the strong electric currents produced by the electron beam. Samples that do not conduct electricity can be damaged by the charges that can build up. Non-conductive specimens must first be coated with a thin layer of conductive material e.g. Au. This coating is accomplished using a sputterer. A sputter coater produces a nanometer thickness of conductive material on the surface through a cold plasma process that retains the contours of the specimen. For samples with a conducting thin film a double sided carbon tape can be used. A link between the thin film and the double sided tape is established using silver paint or the double sided carbon tape itself.

2.4.1.2 SEM Theory

The morphology of ZnO thin films was investigated by the thermionic electron gun SEM (Phillips) XL20. The SEM was operated at 15 keV or 20 keV of accelerating voltage at a 10 mm working distance.

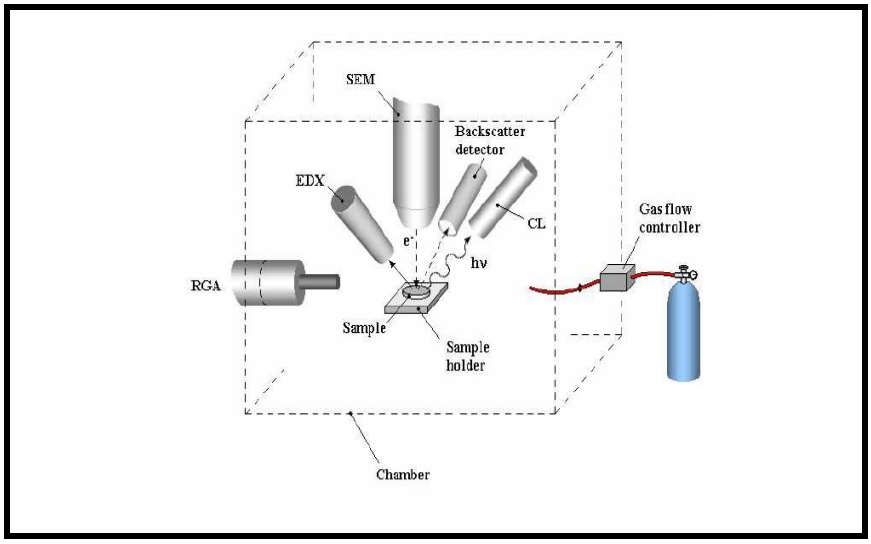

***Figure 2.2**: A schematic representation of how an SEM works showing all the important components for sample characterization **[15]**.*

A thermionic electron gun SEM does not require high vacuum for operation, thus it requires short pump down periods. The as-prepared ZnO substrates were attached on to sample holder of SEM using carbon double sided tape. The SEM was pumped down until a message "VAC OK" was displayed on the operator control window and characterization was carried out.

The SEM uses secondary electrons produced as a result of electron-beam (e-beam) solid interactions to produce a topographic image of the sample. Secondary and backscattered electrons are created during e-beam solid interaction. Electrons that are emitted from the sample with energies below 50 eV are called as secondary electrons while those with energies above 50 eV are called as backscattered electrons. The created secondary electrons are used to obtain SEM images. When the electron beam is rastered across the sample, the emitted secondary electrons

are collected by a detector, and the output can be used to modulate the brightness of a cathode ray tube (CRT) and produce corresponding image **[1].**

By changing the width (w) of the electron beam, the magnification (M) can be changed where

$$M = \frac{W}{w}$$

and W is the width of the CRT. Since W is constant, the magnification can be increased by decreasing w

2.4.2 Energy-Dispersive X-Ray Spectroscopy (EDX)

The EDX system which is interfaced with electron microscopy (SEM, FE-SEM, and HR-TEM). The EDX was used for the composition analysis, presence of thin-film layer, and atomic composition analysis before and after the hydrothermal growth of nanorods arrays on the ZnO thin Film. EDX spectra are obtained by measuring the energy of x-rays emitted from a sample during e-beam bombardment **[16]**.

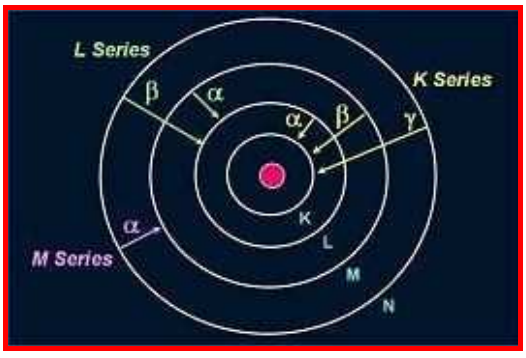

Figure 2.3*: A schematic representation showing how X-rays are produced which are used by the EDX to analyse samples.* ***[16]***

These x-rays are produced as a result of the ionization of an atom when incident electrons remove an inner shell electron. When an ionized atom returns from its excited state to its ground state, an electron from a higher energy outer shell fills the vacant inner shell and then releases an amount of energy equal to the potential energy difference between the two shells. This energy, which is unique for every atomic transition, will be emitted either as an x-ray or as an Auger electron. In EDX analysis, the detector analyzes these emitted x-ray photons from the sample, which can be utilized for quantitative and qualitative composition analysis **[16].**

2.4.3 X-ray Diffraction (XRD)

2.4.3.1 X-Ray Diffraction Sample Preparation.

ZnO thin films deposited by pulsed laser deposition, ZnO nanorods (randon and c-axis orientated) did not require any special treatment before x ray diffraction analysis was performed on them. These samples were attached flat on the stage of the X-ray diffractometer stage using an adhesive.

2.4.3.2 X-ray Diffraction theory

The compound phase of the as-synthesized ZnO thin-films, nanorods, and all samples were identified by x-ray diffraction (XRD) technique. The x-ray diffractormeter used was D8 Advanced Bruker Diffractometer. The standard one-sample-at-a-time reflection holder permits diffraction patterns to be recorded for flat, non-rotating samples in the Bragg-Brentano geometry.

X-Rays from the Copper anode tube are diffracted and focussed by the Vario Ge monochromater onto a focussing slit near the middle of the picture. From here, the beam diverges again to diffract from the sample at the center of the goniometer circle to be detected by the Braun Position Sensitive Detector on the 2θ arm at the right. The sample is pressed flat on the surface of the sample holder. The plane of the holder must rest against three set screws which are arranged in a triangle

2.4.3.3 Bragg's Law

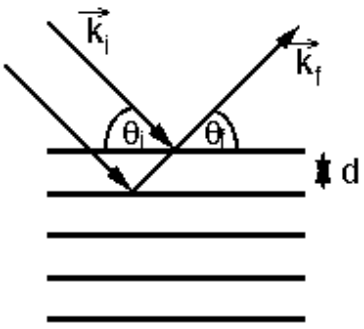

Figure 2.4: *Bragg's Law X-ray diffraction*

$$\theta_i = \theta_f = \theta$$

$$n\lambda = 2d \sin\theta$$

or

$$|\vec{k}_f| = |\vec{k}_i| = \frac{2\pi}{\lambda}$$

$$\vec{q} = |\vec{k}_f - \vec{k}_i|$$

$$= 2k_i \sin\theta$$

$$= \frac{4\pi}{\lambda} \sin\theta$$

$$= \frac{2\pi n}{d}$$

A real 3-dimensional crystal contains many sets of planes. For diffraction, crystal must have the correct orientation with respect to the incoming beam. Perfect, infinite crystal and perfectly collimated beam: diffraction condition must be satisfied ``exactly." Strains, defects, and finite size effects, instrumental resolution: diffraction peaks are broadened.

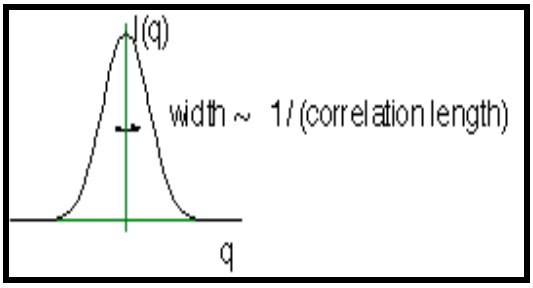

Figure 2.5: *Typical X-Ray diffraction peak*

More formally, the scattered intensity is proportional to the square of the Fourier transform of the charge density:

$$I(\vec{q}) \propto \left| \int d^3r \; e^{i\vec{q}\cdot\vec{r}} \; \rho(\vec{r}) \right|^2$$

Where ρ is the charge density.

For perfect crystals, *I(q)* consists of delta functions (perfectly sharp scattering). For imperfect crystals, the peaks are broadened. For liquids and glasses, it is a continuous, slowly varying function. **[32]**

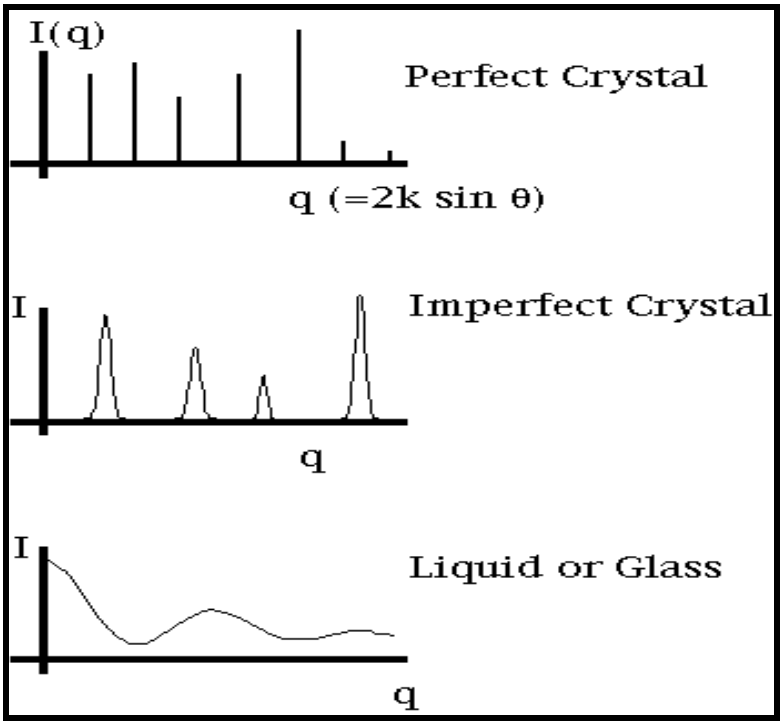

Figure 2.6: *Typical XRD spectra for different materials*

2.4.3.4 Features of X-ray Diffraction

- For a known structure, pattern can be calculated exactly.
- Symmetry of the diffraction pattern given by symmetry of the lattice.
- Intensities of spots determined by basis of atoms at each lattice point.
- Sharpness and shape of spots determined by perfection of crystal.
- Liquids, glasses, and other disordered materials produce broad fuzzy rings instead of sharp spots.
- Defects and disorder in crystals also result in diffuse scattering.

The X-ray diffractometer for this research was operated at 40 kV and 40 mA to generate monochromatic Cu K α x-ray radiation of $\lambda = 1.54$ Å. When a collimated beam of x-rays hit the sample, this beam can be diffracted by the crystalline phases in the specimen according to Bragg's law towards the sample detector [**17]**.

The movement of the sample detector is controlled by an external computer. Signals from the detector are then fed into the computer for analysis. The intensity of the diffracted x-rays was measured as a function of the diffraction angle (2θ).

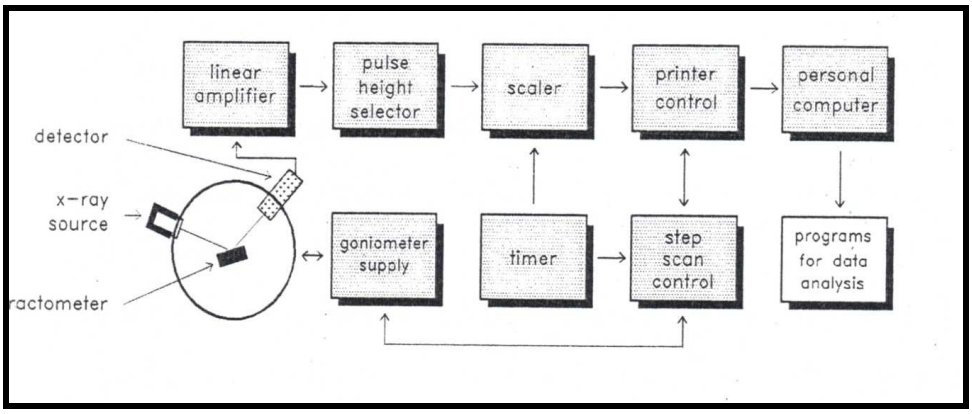

Figure 2.7**: Important components of the x-ray diffractometer **[17].

2.4.4 RUTHERFORD BACK-SCATTERING TECHNIQUE (RBS)

RBS was used for the the relative atomic composition and thicknesses of ZnO thin films deposited. Rutherford back-scattering technique (RBS) is an analytical tool that uses elastic scattering of 0.1-3 MeV charged particles to analyze the surface and the outer few micrometers of solids **[26].**

A typical RBS system consists of an accelerator and scattering chamber with sample manipulators and particle detectors. In an RBS system the samples are bombarded with 1-3 MeV protons or alpha particles from a Van de Graaff electrostatic accelerator and the scattered particles are detected by surface barrier detector**.**

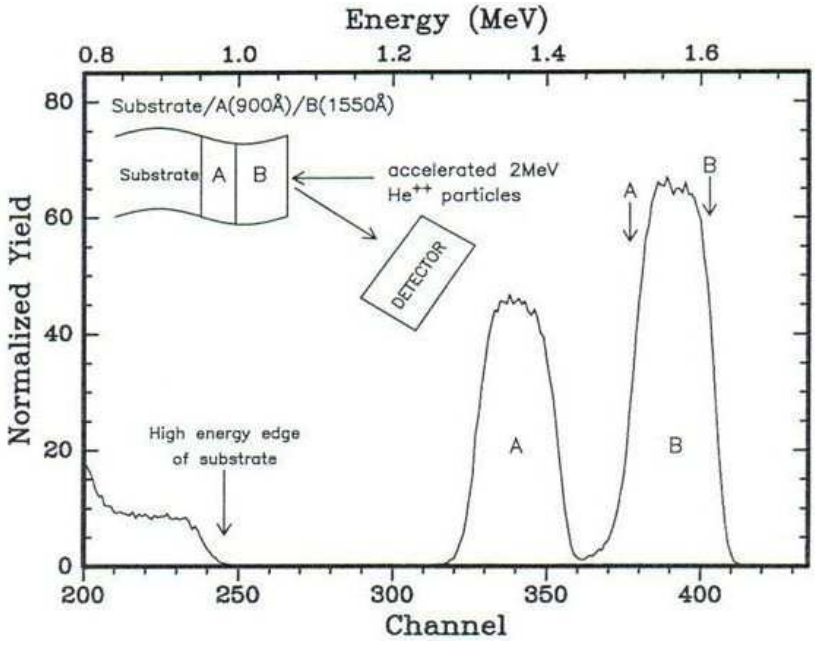

Figure 2.8**: Backscattering spectrometry. The insert diagram shows a sample with the following profile: Substrate/ A (900 Å)/ B (1500 Å). 2MeV He+ particles scatter from the sample onto the detector. The spectrum shows a plot of the number of counts (or Yield) as a function of energy of the scattered particles. The arrows indicate the surface position energies for elements A and B. These position are dependent on the atomic mass, while the counts are dependent on the square of the atomic number i.e. Z^2* ***[17].

The signal from the detector is processed by common nuclear electronics and the particle energy spectra are stored in a computer based multi channel analyser. The data evaluation is accomplished using standard procedures and computer codes. The advantage of the RBS technique lies in the quantitative analysis of major and minor constituents lying in the first 0.5 to 2.0 micrometers of a material. Depending on the sample structure and composition, the detection limits vary from 10^{11} to 10^{15} at.cm^{-2} for heavy and light elements respectively. The detection limits for some light elements may further be improved by using resonant scattering. The depth distribution of constituents can be reconstructed with a depth resolution of 10-20 nm **[26]**.

The RBS technique is non-destructive since the erosion and the radiation degradation of the sample material by the particle impact is negligible. Since the samples are situated in vacuum the possibility of RBS analyses of materials comprising volatile components is strongly limited. The most extensive use of the RBS technique is in the field of electronical and optical materials, special coatings and in the study of various physico-chemical processes on the solid surfaces.

Back-scattering spectrometry using a monoenergetic (2MeV) and collimated beam of $^4HE^+$ particles together with a computer aided simulations of RBS were used to determine:

- The relative atomic composition i.e. stoichiometry of the compounds/phases of the thin ZnO films deposited on glass substrates.

Identification of the atomic mass of the target elements i.e.

$E_\alpha\alpha$ mass

The determination of the distribution of the target elements as a function of depth below the surface i.e. $\frac{dE}{dx}$ is the depth scale.

The scattering cross section, σ where

$\sigma \alpha Z^2$

$^4He^+$ particles scatter elastically from target atoms with energies characteristic of the mass of the struck particle. They lose energy as they pass in and out of the material film. Energy analyses of the back scattered $^4He^+$ particles by the detection system yields the backscattering spectrum

shown in the lower diagram in the form of counts per channel versus channel number. The channel number is linearly related to the backscattered energy E_1. appearing in the spectrum is a nearly flat topped peak of each element present in the film. The peak widths are caused by the energy loss of the alpha particles.

The film elements may be identifies by insertion of the measured energies of the ($E_1^A ; E_1^B$) high energy sides of the peaks into

$$K_i = \frac{E_1^i}{E_0}$$

to calculate the kinematic factor K for the i^{th} element. E_o is the incident ion's laboratory kinematic energy. Application of the conservation of energy and the momentum leads to the kinematic factor K being given by

$$K = \left[\frac{\left(M^2 - m^2 \sin^2 \theta \right)^{\frac{1}{2}} + m \cos \theta}{M + m} \right]^2$$

where θ is the laboratory angle through which the incident ion scattered and m and M are masses of the incident and target particles respectively. Since the parameters m, Eo and θ are usually known, M is determined and the target element is identified if t is the film thickness and N_i the atomic density of the i th elements, then (Nt)i is the areal density, given by

$$(Nt)_i = \frac{A_i \cos\theta_1}{Q\,\Omega\,\sigma_i(E,\theta)}$$

A_i is the integrated peak count for the Q ions which are incident at angle θ_1. Ω is the detector solid angles and σ_i the cross section.

The average stoichiometric ration for the compound film A_xB_y is given by.

$$\frac{y}{x} = \frac{N_B}{N_A} = \frac{A_B}{\sigma_B}\frac{\sigma_A}{A_A}$$

In this equation, the hard to measure quantities of Q and Ω have cancelled. Given that the film density is ρ_{AB}

And that $M_{AB} = xM_A + yM_B$ is the molecular weight of the compound A_xB_y, we have

$$N_A^{AB} = \frac{x\rho_{AB}A_V}{M_{AB}}$$

And

$$N_B^{AB} = \frac{y\rho_{AB}A_V}{M_{AB}}$$

Where A_V is Avogadro's number and N_A^{AB} the atomic density of A in the compound AB, N_B^{AB} the density of B in compound AB. Thus

$$t = \frac{(Nt)_A}{N_A^{AB}} = \frac{(Nt)_B}{N_B^{AB}}$$

1-2 MeV ^{4}He ions will be used for the preceeding analysis for the following reasons:

- Data for the energy loss of ^{4}He ions in the elements are better known than for other ions.

- The silicon surface barrier detector energy resolution for 4He is about 15keV.

- The backscattering cross-section for ^{4}He ions incident on all elements more massive than Be are nearly all Rutherford in this energy region.

The principal strengths of Rutherford backscattering with ^{4}He ions are:

- It is an absolute method in that is does not require the use of standards.

- It is quick and easy; typical data acquisitions is about 10 minutes.

- It is frequently non-destructive

- It may be used depth profiling, with 10-30 nm resolution

The principal failure of this technique is its failure to analyse trace elements.

For fixed θ , the energy separation ΔE , for beam particles scattered by target particles of mass M is.

$$\Delta E = E_0 \left(\frac{dK}{dM} \right) \Delta M$$

If ΔE is set equal to δE , the minimum energy separation that can be experimentally revolved, then δM , the mass resolution of the system is

$$\delta M = \frac{\delta E}{E_0 \left(\frac{dK}{dM} \right)}$$

δE contains contributions from the detector resolution, straggling, beam energy spread and various geometric effects.

The mass resolution at the samples surface is determined mainly by the detector resolution. For deeper layers, straggling dominates.

The average differential cross section, $\sigma(\theta; E)$ for scattering of beam particles of energy E by target particles in a thin film is defines by

$$\sigma(\theta; E) = \left(\frac{1}{Nt} \right) \frac{dQ(E)}{Q} \frac{1}{\Omega(\theta)}$$

Where Nt is the number of target atoms/unit area perpendicular to the beam, and $\frac{dQ(E)}{Q}$ is the fraction of the incident particles scattered into the small solid angle $\Omega(\theta)$ centred at the deflection angle θ.

If scattering is Rutherford (pure Coulomb), then scattering cross section

is $$\sigma_R(E,\theta)=\left(\frac{Z_1Z_2e^2}{4E}\right)^2\times\frac{4\left[\left(M^2-m^2\sin^2\theta\right)^{\frac{1}{2}}+M\cos\theta\right]^2}{M\sin^4\theta\left(M^2-m^2\sin^2\theta\right)^{\frac{1}{2}}}$$

Where Z_1 and Z_2 are the atomic numbers of the incident and the target atoms respectively. This equation is in cgs units with

$$e^2 \approx\sim 1.44\times10^{-12}\,MeVcm$$

An accurate approximation for large backscattering angles and $\frac{m}{M}$ 1 is

$$\sigma_R(E,\theta)\approx 0.02073\left(\frac{Z_1Z_2}{4E}\right)^2\left[\sin^{-4}\left(\frac{\theta}{2}\right)-2\left(\frac{m}{M}\right)^2\right]$$

The IBM and Cornell geometrics are the common experimental arrangements. For both geometrics the incident beam is horizontal and the sample surface is vertical. In the IBM geometry, the scattered beam (directed at the detector) and the incident beam are in the same horizontal plane. **[17]**

In the Cornell geometry, the incident and scattered beam are in the same vertical plane, with the detector directly below the incident beam. In both geometries the angle between the scattered beam and the sample normal is θ_2. The tilt axis is a vertical axis through the beam spot on the

sample surface. θ_1 is the tilt angle. For the IBM geometry, $\theta = \pi - |\theta_1 \pm \theta_2|$. For the Cornell geometry $\cos\theta_2 = \cos(\pi - \theta)\cos\theta_1$

CHAPTER 3

3. THE DESIGN OF THE GAS TESTING CHAMBER

3.1 Introduction

To effectively test the effects of temperature on the sensitivity of the sensor to the test gas, the gas testing chamber was designed. The chamber had to be capable to retaining gas inside it, since test gases used were extremely explosive in nature. The body of the chamber was made from brass. The chamber was designed in such a way that will make the constant monitoring of the sample and temperature possible. The lid of the chamber had a window for sample monitoring to ensure that, all connections for temperature and resistance measurements were always intact.

3.2 The designing Process

A stage capable of heating up to a desired temperature was designed during this research. This stage was used to heat up the sample to a desired test temperature, see item 1 in **Figure 3.1**. The temperature of the stage was controlled by adjusting the supply voltage from the power supply using the calibration table. The stage was made up of six, 33 k.Ω resistors with a power rating of 10 W.

The test gas inlet was used to introduce 20 % test gas (hydrogen/ acetylene), **part no. 2, Figure 3.1,** i.e (20 vol% of test gas) inside the chamber, for test purposes. To monitor the amount of gas entering the chamber gas regulators were used for each gas used for this research. The nitrogen pipe inlet was used to introduce 80% nitrogen i.e 80 vol% of the carrier of the carrier gas inside the chamber. A thermo-couple was used to monitor the temperature of the stage. For the removal of gases contained inside the chamber, a pipe from the gas outlet was immersed into water, to reduce an explosion risk. Ag contacts were used to connect wires to the Tru-RMS multimeter used for measuring the test gas effects on the resistance of the samples. A lid with a window was used to close the chamber and monitor all connection to samples and the thermocouple. Several substrates were essayed for this research, i.e. ZnO thin-films without ZnO nanorods, ZnO thin-films with ZnO nanorods and Finally ZnO thin-films with nanorods that are doped with Pb respectively.

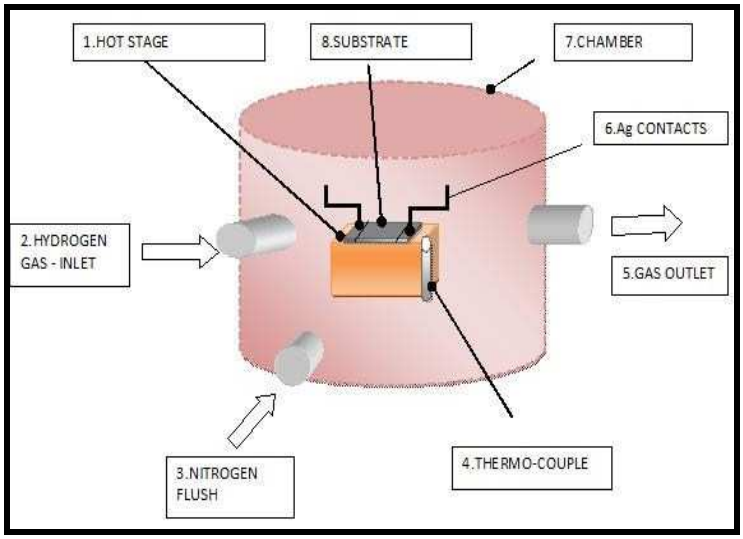

Figure 3.1*: Schematic diagram of the gas testing chamber built for the study of gas sensing characteristics of ZnO nanorods.*

In **Figure 3.2** most of the components labelled in **Figure 3.1** can be seen, through the window on the lid, the ZnO thin film sample can be seen sitting on top of hot white resistors with multimeter connection. The gas pipes are also visible on the sides of the chamber.

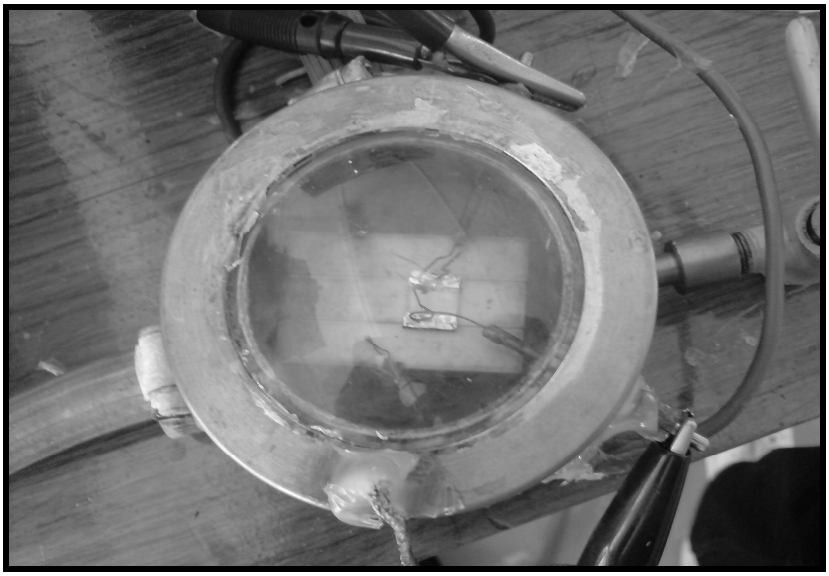

***Figure 3.2**: The gas chamber that was used for tests conducted of samples using test gases.*

***Table 2**: Temperature Calibration table for the gas sensing chamber*

Voltage(V)	**Current(A)**	**Temperature(^{o}C)**
0	0	25
5	0.93	60
10	1.85	131
15	2.75	268
17	3.13	350
22	3.5	400

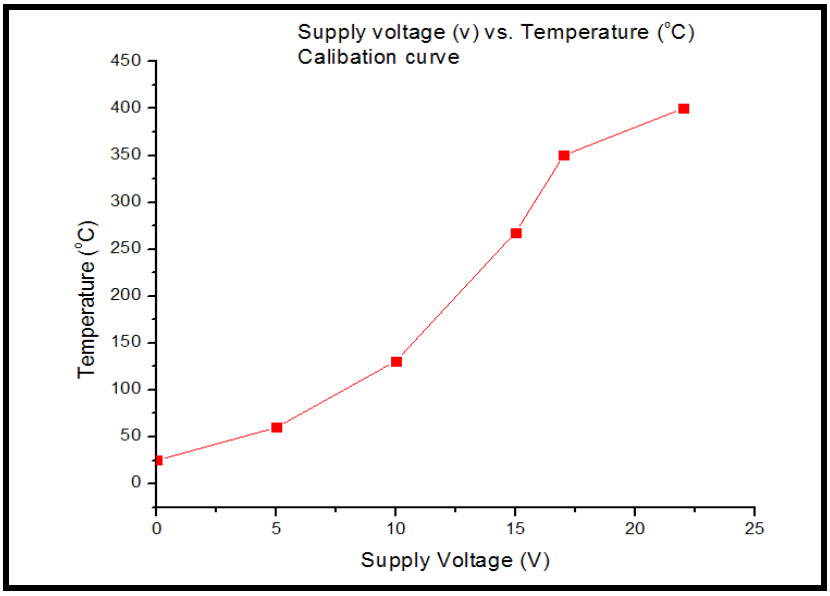

Figure 3.3: *The graph of supply voltage vs. temperature for the test cell*

The temperature-supply voltage relationship was calibrated, which is the dependence of stage temperature on the supply voltage. The calibration was done to ensure easy temperature modifications, during experiments. Other values not included in the table see **Table 2 and Figure 3.3.** , were estimated using the linear relationship between the supply voltage and the sample stage temperature.

A typical layout of the samples used for gas sensing in this study in represented in **Figure 3.4**, with all the typical components and connections

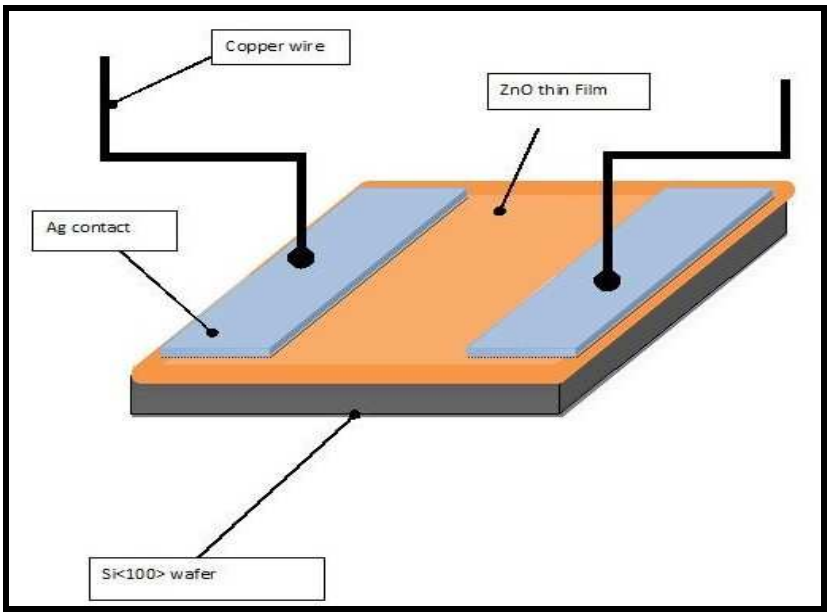

***Figure 3.4**: A schematic representation of the sample that may be used for gas sensing application.*

3.3. Gas sensitivity testing Process

Substrates with Ag contacts were placed on the heating stage. Wires from the multi-meter were connected on the sample using Ag contacts for resistance change measurements. After closing the testing chamber the temperature of the sample was increased to the desired testing temperature, which varied between 100-400 ^{o}C. When the desired testing temperature was reached a steady flow of 80ml/min of Nitrogen was introduced, as the carrier gas. When the resistance of sample was stable 20 ml/min flow of a test gas (Hydrogen or Acetylene) was introduced into the chamber. Immediately after the introduction of a test gas, the resistance vs. time reading were taken using the Tru-RMS multimeter. The Tru-RMS multimeter is capable of taking readings every second. The readings obtained were used to plot graphs of resistance (Ohm) versus time(s). From the Resistance vs. time graphs of each test temperature, the

sensitivity and response time were calculated and measured respectively. The sensitivity percentage of the sensor at each temperature was defined as 100x [(R_{air}, - R_{gas}) / R_{air}] where R_{gas} is the resistance of the sensor in a test gas and R_{air} is the resistance of the sensor in air (Nitrogen). For this study the response time of the sensor was defined as the period of sharp resistance decrease immediately after the introduction of the test gas. This is the region before the sensor begins to reach equilibrium and starts to stabilise.

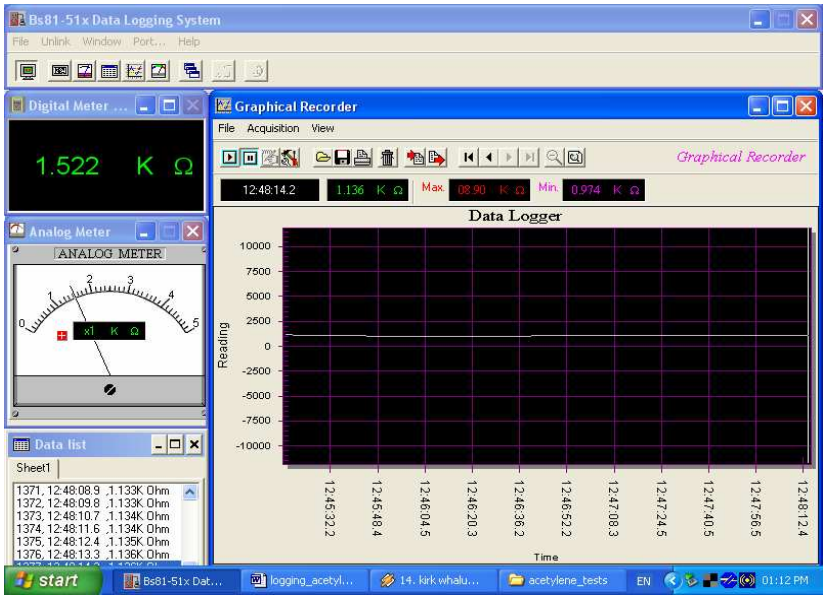

***Figure 3.5**: Computer interface of the true-RMS multimeter that was used for taking changes in resistance as the gas is introduce*d.

The screen view of the software used for taking resistance measurements from the Tru-RMS multimeter. The data logger plots the data obtained from the True-RMS see **Figure 3.5**. Data from this software can then be exported as a spreadsheet file, and a desired programme capable of reading spreadsheet files can be used to plot graphs.

CHAPTER 4

4. ZNO THIN-FILMS DEPOSITED ON GLASS SUBSTRATES BY PULSED LASER ABLATION (PLD)

4.1. Introduction.

This chapter presents results obtained from ZnO thin-films deposited by Pulsed Laser Deposition. ZnO 99.999% from industrials Analytical (PTY) LTD was used to make target pellets for the Pulsed Laser Deposition system. The pellets were made using a pressure pellet maker. The structural and morphological characteristics were characterized using X-Ray Diffraction and Scanning Electron Microscope equipped with EDX. After characterization, hydrogen and acetylene gas sensitivity tests of ZnO thin-films were carried out using the gas testing chamber set-up and the Brymen TBM 812 tru RMS multimeter for resistance measurements.

4.2 Experimental

4.2.1 Pulsed laser thin film deposition

Glass slides were cut into 100mm^2 square glasses and used as substrates. The substrates were cleaned using the standard cleaning procedure: methanol, acetone, trichloroethylene, acetone, methanol and finally deionised water. The stirring was carried out using an ultrasonic bath. After finishing the cleaning procedure, the samples were then dried in air. After drying, thin films of

ZnO were deposited on these bare glass substrates without any further treatment, using Pulsed Laser Deposition. The target used for ZnO deposition was a pellet with a diameter of 12 mm and a thickness of 3 mm. The pellets were made from 99.999% zinc oxide powder obtained from Industrial Analytical. The laser voltage was 500 mV.

The repetition rate was set at 10Hz. The area covered by the laser when hitting the target was approximately 0.117 cm^2. The energy of the laser was 250mJ and the energy density was 2.12 J/cm^2. The target distance was set at 5cm (defined as the distance between the substrate and the target). The base pressure used for all experiments was 5×10^{-5} mBar.

When this base pressure was achieved, oxygen gas was introduced until the working pressure of 300 mBar was achieved. Oxygen was used as the background gas to ensure that the ZnO thin films deposited were fully oxygenated. During deposition, the target was rotated and rastered to ensure that the laser does not hit the same spot on the target. The number of laser pulses used for all samples was 30000. The temperature of the substrate holder was varied between 150 ^oC and 300 ^oC. Thin films deposited were used for both gas sensing and as seeds for orientated ZnO nanorods growth.

4.3 Results and discussions

4.3.1 Scanning Electron Microscope and EDX.

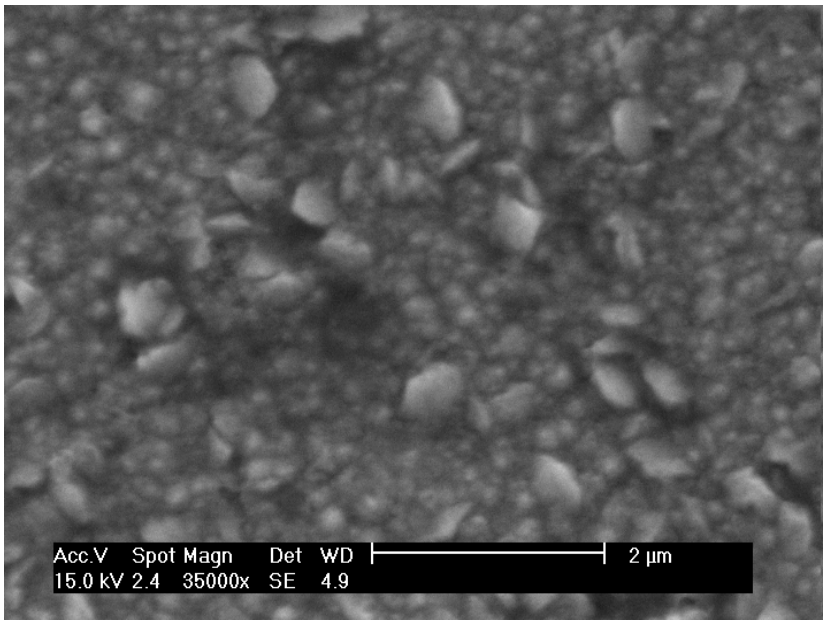

Figure 4.1*: SEM image of the ZnO thin film that was deposited by Pulsed laser deposition with 30000 shots (Laser Pulses).*

The morphology of ZnO thin films deposited by Pulsed laser deposition was found to be very rough and the size of particles was not uniform see **Figure 4.1**. As a result of different grain sizes of ZnO seeds forming the ZnO thin film, orientated ZnO nanorods deposited on these films were also expected to have a large variety of diameters, with smallest ZnO seed causing the growth, of a ZnO nanorod with the smallest diameter, and the biggest ZnO seed causing the opposite.

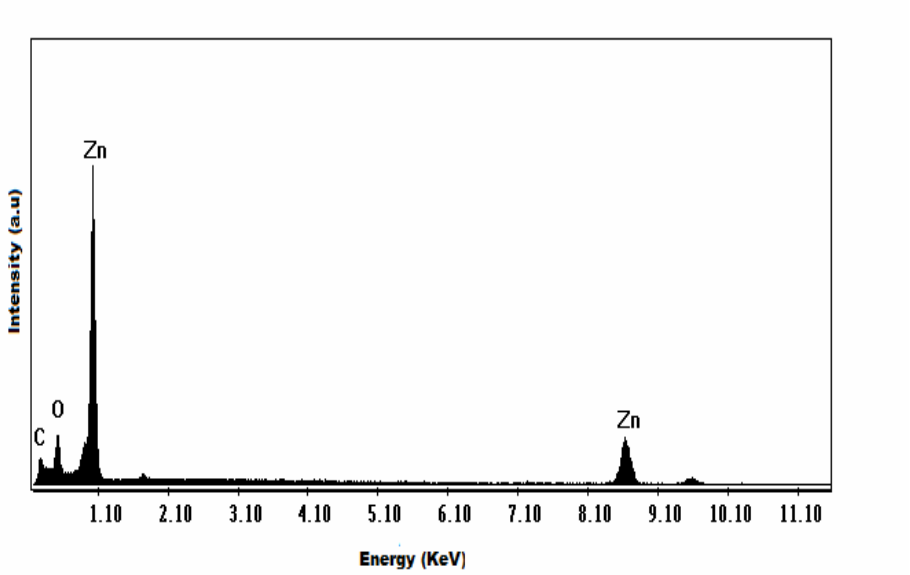

***Figure 4.2**: EDX, analysis of the as-deposited ZnO thin films using Pulsed laser deposition*

The EDX analysis performed on the deposited thin films showed the presence of zinc and oxygen only, see **Figure 4.2**. There were no impurities recorded by EDX on the as deposited ZnO thin films. The presence of carbon was caused by the double sided carbon tape that was used to mount samples on the SEM stage.

4.3.2 X-Ray Diffraction

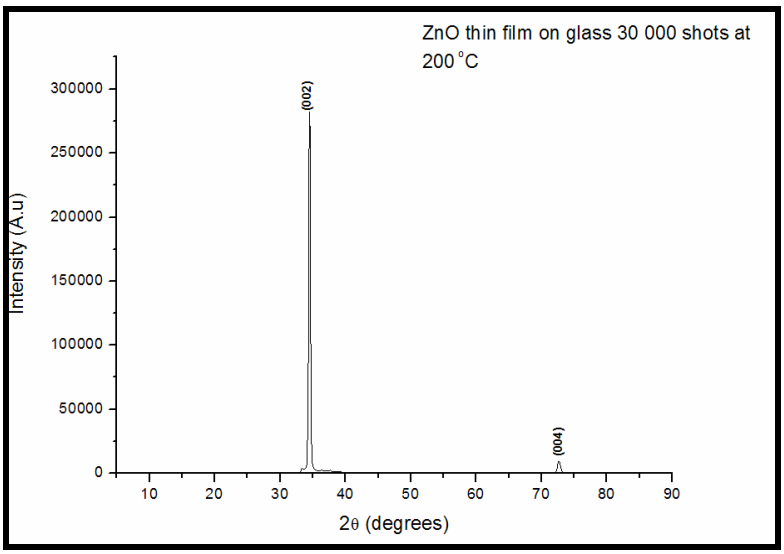

***Figure 4.3**: Shows an XRD pattern of a ZnO thin film deposited on glass at 200°C*

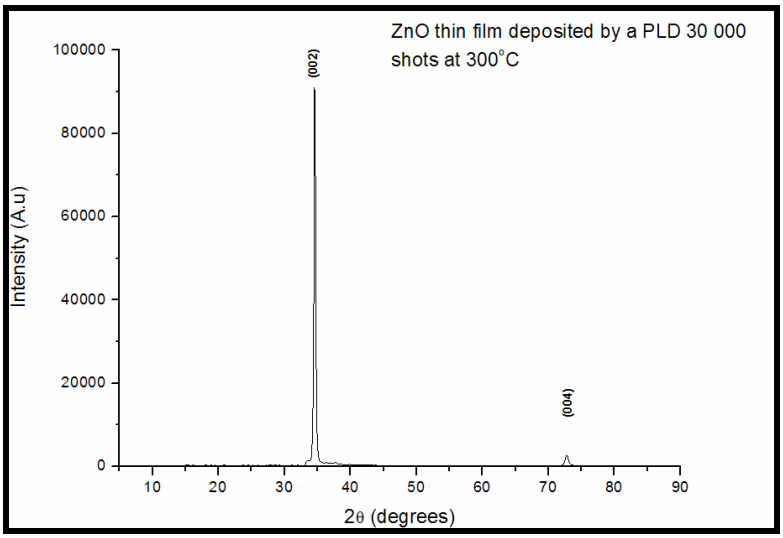

***Figure 4.4**: Shows an XRD pattern a ZnO thin film deposited on glass at 300°C.*

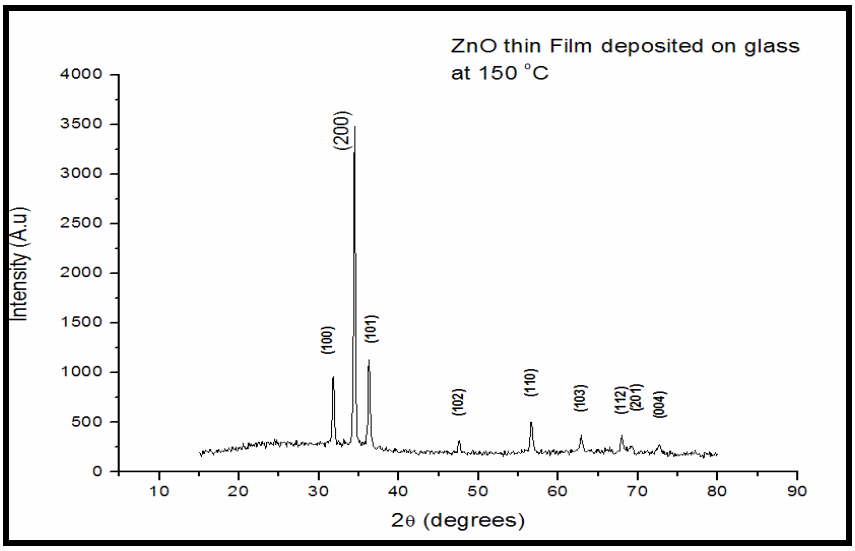

***Figure 4.5**: XRD pattern of a ZnO thin film deposited on glass at a temperature of 150^{o}C*

Figures 4.3 and 4.4 show X-ray diffraction spectra of ZnO thin films deposited using PLD at 200 and 300 ^{o}C respectively. The crystal structure of samples deposited at these temperatures showed excellent orientation along the c- axis, with only peaks belonging [002] planes family appearing. Thin films deposited at 150 ^{o}C, see **Figure 4.5,** showed good orientation along the c-axis; however other peaks besides (002) plane family were more visible, as a result nanorods grown on these thin films were not expected to grow perfectly along the c-axis.

4.3.3 Rutherford Backscattering

Rutherford Back-Scattering spectrum, see **Figure 4.6**, showed a good fit with the simulated ZnO spectrum. From this data it can be concluded that the ZnO thin-films deposited using PLD were perfect stochiometric ZnO. From the RBS spectrum the thicknesses of thin films deposited was found to be approximately 10-13 µ.m

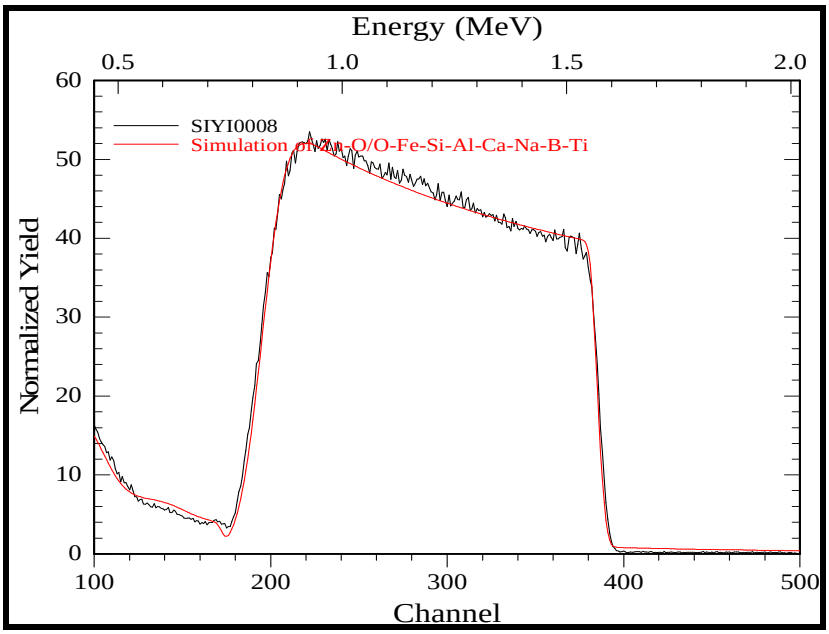

***Figure 4.6**: RBS spectrum of the as-deposited ZnO thin films using Pulsed Laser deposition.*

4.3.4 Gas sensing properties

The gas sensing properties of ZnO thin films deposited were investigated for both test gases (acetylene and hydrogen). ZnO thin films were found to have poor sensitivities at lower temperatures and could not sense acetylene in the greatest segment of the temperature test range.

4.3.4.1 Hydrogen gas sensing of ZnO thin films

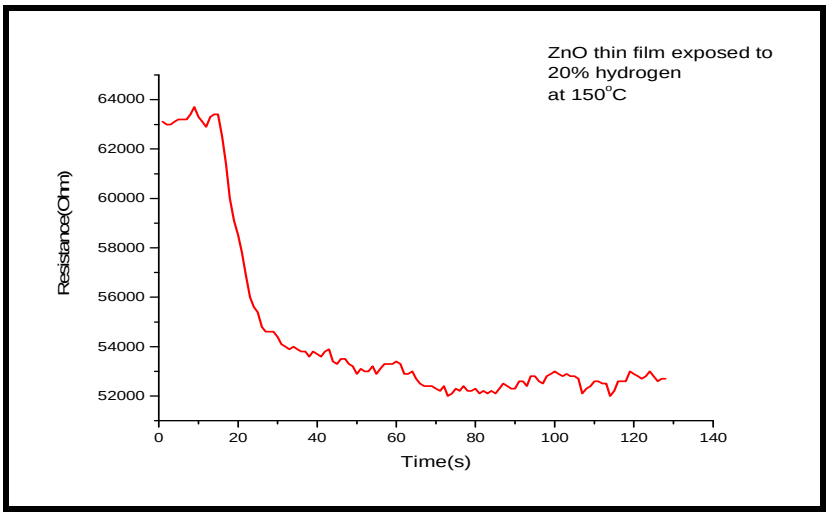

***Figure 4.7**: ZnO thin film exposed to hydrogen at 150°C*

When a ZnO thin film with Ag contacts was exposed to 20% hydrogen at 150 °C, the response time of the sensor was 19 s, see **Figure 4.7**. During this period the resistance of the thin film dropped from 63 to 54 k.Ω and it sensitivity was 13 %. However when the hydrogen was switched off during the resistance stabilization stage, the resistance of the thin film did not recover to its original value. The poor recovery of the thin film at 150 °C showed that ZnO thin films deposited by PLD are permanently reduced when they are exposed to hydrogen at 150 °C. Because of permanent reduction, a ZnO thin film based gas sensor cannot effectively function at this temperature for hydrogen sensing.

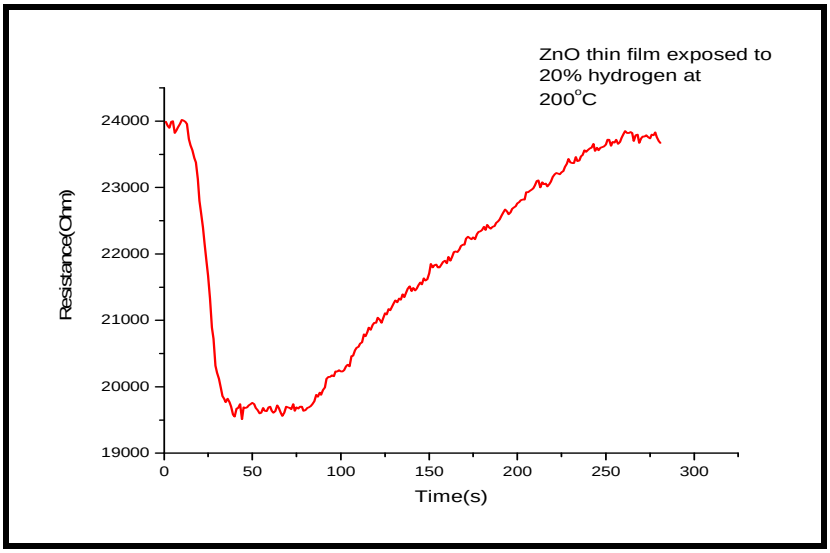

***Figure 4.8**: ZnO thin film when exposed to 20% hydrogen at 200°C*

At 200 °C the response time was discovered to be 21 s, see **Figure 4.8**. The resistance of the sample decreased from 24 k.Ω to 20 k.Ω, as a result, at this temperature the sensitivity was found to be 17%. The recovery time of the sensor was 177 seconds.

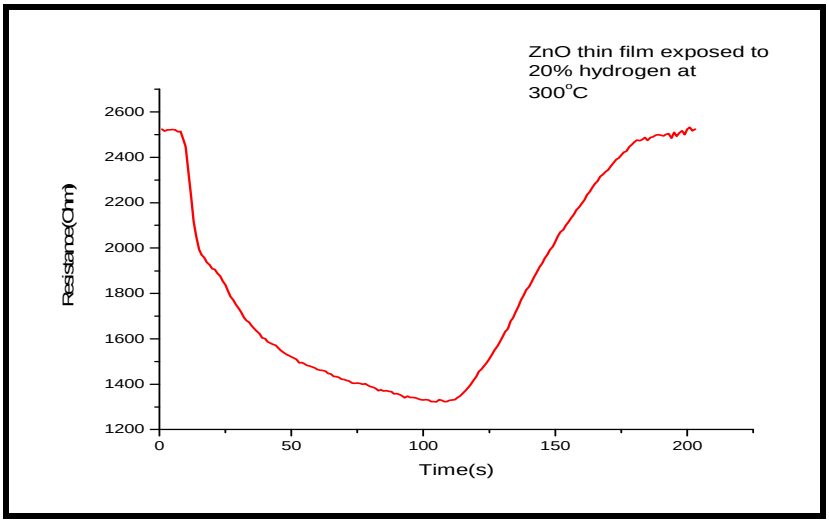

***Figure 4.9**: ZnO thin film at a temperature of 300°C, exposed to hydrogen.*

The response time of the ZnO thin film gas sensor when exposed to hydrogen at 300^{o}C, was found to be 22 s, see **Figure 4.9**. The resistance of the sensor decreased from 2515 to 1347 Ω and its sensitivity was 46 %. The recovery time was found to be 70 seconds.

The response time was found to be 17 s, for a ZnO thin film exposed to hydrogen at 350 ^{o}C, see **Figure 4.10**. The better response time compared to lower temperatures was due to the fact that at higher temperatures the number of active sites for the adsorption of atomic hydrogen increases. The resistance of the sample decreased from 1361 to 457 Ω, as a result, the sensitivity of the sensor at this temperature was 66%. The recovery time was found to be 40 seconds. For the temperature range investigated in this study, this temperature was found to be the optimal temperature with superior, sensitivity, response and recovery time.

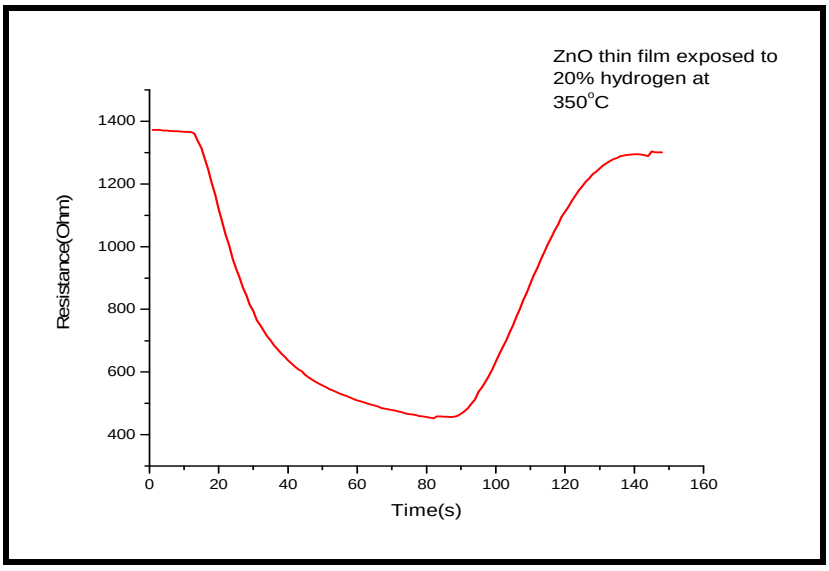

***Figure 4.10**: ZnO thin film exposed to hydrogen at 350^{o}C*

At 400 ^{o}C the response time for the ZnO thin film exposed to 20 % hydrogen was found to be 20 seconds, see **Figure 4.11.** At this temperature, the sensor took longer to reach the stabilization state. The resistance of the sensor during this period decreased from 966 to 298 Ω, the sensitivity was found to be 69 %. The recovery time of the thin film sensor was found to be about 59 s.

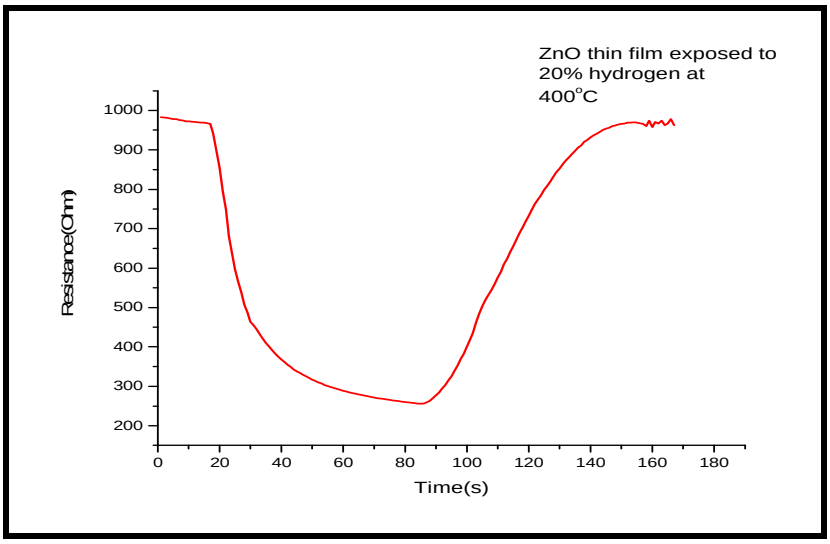

***Figure 4.11**: ZnO thin film exposed to 20 % hydrogen at 400^{o}C*

The sensitivity at the lowest temperature 150^{o}C was found to be poor due to fewer species of hydrogen ions attached to the active sites on the thin-film sensor (hydrogen H^{+} ions attached to the O-polar end of the ZnO wurtzite cause a decrease in resistance of ZnO thin-films) ,see **Figure 4.12**. The sensitivity gradually increased as the temperature was increased. Above 350 ^{o}C the slope of sensitivity began to decrease due to saturation of available adsorption sites on the ZnO thin film meaning the available sites were no longer increasing exponentially with temperature as they did at lower temperatures.

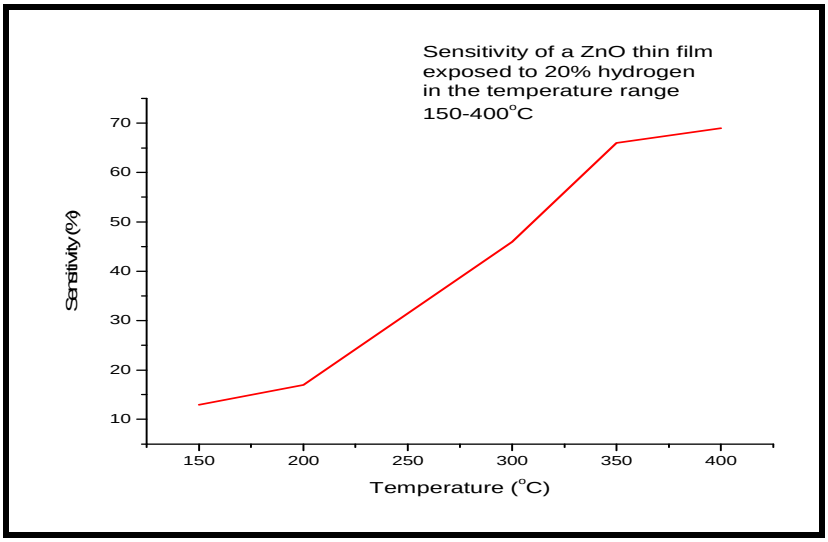

***Figure 4.12**: Sensitivity of ZnO exposed to hydrogen at different temperatures*

From the variation of sensitivity with temperature graph, seen in **Figure 4.12,** it was concluded that a ZnO thin film gas sensor functioned at its optimum in the temperature range 300-350 ^{o}C. This was proved by superior, sensitivity, response time and recovery time found within this temperature range.

4.3.4.2 Acetylene gas sensing of ZnO thin films.

Tests performed on ZnO thin-films with thicknesses of approximately 10 microns using acetylene as the test gas showed that acetylene cannot be effectively sensed using a ZnO thin-film based sensor at temperatures lower 400 ^{o}C. When gas sensitivity tests for acetylene were performed at these temperatures, the resistance of the sensor did not show any noticeable change in resistance.

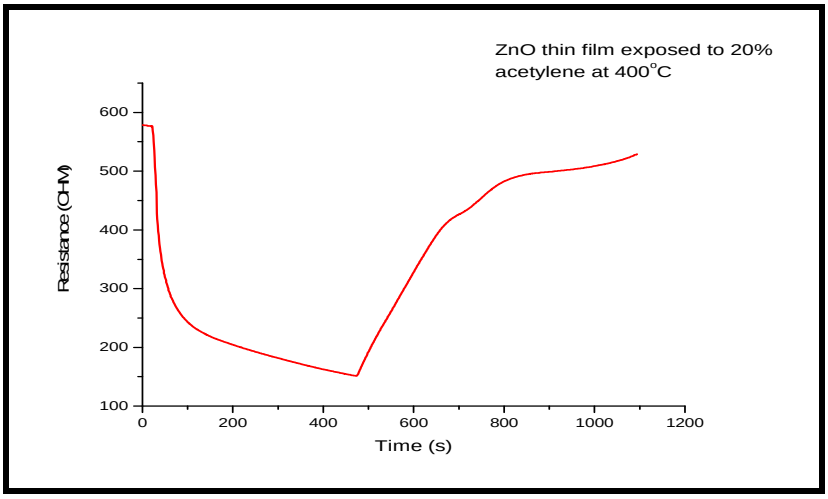

***Figure 4.13**: Represents the response of the ZnO thin film to acetylene at 400 °C.*

When 20 % acetylene gas in nitrogen was introduced into a ZnO thin film sensor at 400 °C, unlike lower temperatures this temperature caused a noticeable decrease in the resistance of the sensor. The resistance of the ZnO thin film decreased sharply, after 25 seconds it was almost half of its initial value, see **Figure 4.13**. The thin film gas sensor started to stabilise after 30 seconds. The temperature of 400 °C is very high and the sensor's response time at this temperature is long. The recovery time of the sensor was found to be 5 minutes or 300 seconds. Both recovery and response times are not ideal for applications in the flammable gas sensing industry, as the sensor would take too long to sense leaks and recovery from each sensing event.

CHAPTER 5

5. ZnO NANORODS ON BARE Si <100> SUBSTRATES

5.1 Introduction

This chapter presents results obtained from the ZnO nanorods which were synthesized by hydrothermal synthesis on bare silicon substrates (substrates without ZnO thin films /nanorods seeds). The precursor solutions for hydrothermal synthesis were prepared (1) Zinc Chloride and aqueous ammonia and 2) using zinc nitrate and hexamethylenetetramine (HMT). The structural properties and microstructure of the ZnO nanorods synthesized at various experimental conditions were characterized using XRD and SEM equipped with EDX. The experimental conditions were varied to get the optimal experimental conditions for the fabrication of the gas sensor.

5.2 Experimental

Single crystal silicon Si<100> was used as a substrate. Samples were cut from 626 µm thick Si<100> wafers into small squares of about 10x10 mm^2 in dimensions. The as-cut Si<100> pieces were chemically cleaned with methanol, trailed by acetone, then trichloroethylene, acetone, methanol and lastly deionised water. The stirring was carried out using an ultrasonic bath. After the cleaning procedure was complete the samples were then dried in air.

5.2.1 ZnO nanorods prepared using Zn $(NO)_3$. $6H_2O$ and HMT

ZnO nanorods were synthesized by a thermal decomposition of a zinc-amino complex under hydrothermal condition. Glass bottles (DURAN) with rubber caps were used as reactor vessels (120 ml) **Figure 5.1**. Zn $(NO)_3.6H_2O$ and $C_6H_{12}N_4$ purchased from Industrial Analytical (PTY) LTD were used without any further purification. Equi-molar aqueous solutions of zinc nitrate hexahydrate ($Zn(NO)_3.6H_2O$)) and hexamethylenetetramine (HMT, $C_6H_{12}N_4$) were prepared, Si <100> substrates were then placed into the solutions and heated at a constant temperature of 90°C in an oven for 8,12, and 18 hours. After the set time points were reached, samples were removed from autoclaves and thoroughly washed using deionised water to remove the amino and salt residues formed during deposition. The washing step for the samples was trailed by drying in air. The concentration of the precursor solutions varied between 0.001 to 0.1 M to investigate the effects on ZnO nanorods morphology and surface coverage.

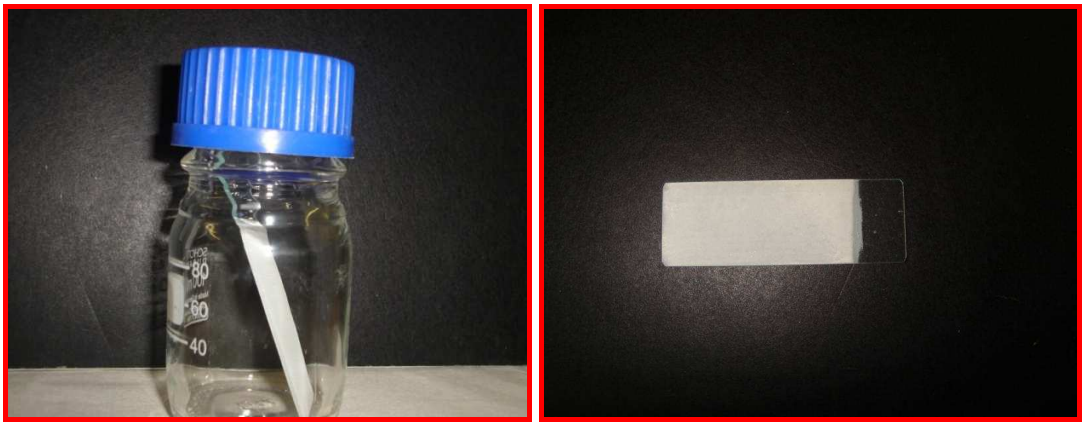

Figure 5.1*: Bottle with an autoclavable cap. Inside the bottle is a tilted microscope slide that was used for deposition of ZnO nanorods b) shows the microscope slide as it looked after deposition ZnO nanorods.*

5.2.2 ZnO Nanorods prepared using Zinc Chloride and Aqueous Ammonia

These ZnO nanorods were also synthesized by a thermal decomposition of a zinc-amino complex under hydrothermal condition. Glass bottles (DURAN) with a rubber cap were used as reactors (120 ml). In this method zinc chloride and aqueous ammonia purchased from Industrial Analytical (PTY) LTD were used. The concentration of Zinc Chloride $ZnCl_2$ was varied between 0.005 and 0.5 M. In each concentration case, aqueous ammonia was slowly added while stirring to alter the initial PH of the solution. The initial PH of the solution was varied between 9.4 and 13.5, this was done investigate its effects on the morphology and the density of nanorods on the substrate.

5.3 Results and discussions

5.3.1 X-RAY Diffraction

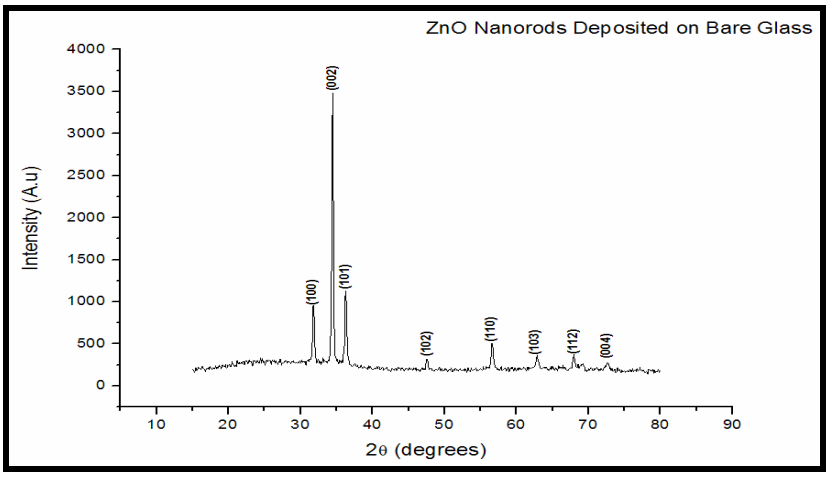

***Figure 5.2**: XRD pattern of ZnO nanorods deposited using Zn $(NO_3)_2$ and HMT*

The X-Ray Diffraction pattern for all samples revealed a hexagonal wurtzite phase of well crystalline ZnO see **Figure 5.2**. The presence of other planes except the (002), resulted from nanorods stacking on top of each other, due to the absence of ZnO seeds, which are used to cause growth along the c-axis as a preferred plane orientation.

When Zinc nitrate and HMT were used to prepare a precursor solution for ZnO nanorods deposition on bare Si<100> substrates, they required longer periods for good precipitation to occur. The concentration that yielded the best ZnO nanorods density evenly all over the substrate surface was 0.01 M, the deposition time was 18 hours. This optimum concentration for zinc chloride + HMT is the concentration that was used when Pb-doped ZnO nanorods were prepared in Chapter 7.

The precursor solution prepared using Zinc chloride and aqueous ammonia gave good surface coverage with relatively shorter deposition time. The reason for shorter deposition periods that yield good substrate coverage can be attributed to a more efficient degradation of aqueous ammonia to form ammonia and the differences between the initial and the final PH. The optimum concentration and PH for aqueous ammonia and zinc chloride was found to be respectively 11.2 and 0.05 M. This optimum PH and concentration was used to prepare orientated undoped-ZnO nanorods in chapter 6.

5.3.2 Scanning Electron Microscope and EDX

ZnO particles prepared using different concentrations yielded different morphologies and surface coverages. While ZnO nanorods, prepared using an equimolar concentration of 0.001 M for zinc nitrate and HMT showed poor surface coverage and required extended periods for deposition, the ZnO nanorods prepared at 0.01 M had a relatively good surface coverage showing the dependence of surface coverage on concentration. See **Figure 5.3** (a) shows ZnO nanorods which were prepared at 0.001 M equi-molar solution, (b) is a closer look at one of the as-deposited nanorods which shows nanorods growing on top of each other resulting in star-like structures called multipods, there has been reports of multi-pods being used as gas sensors **[9]**, (d) ZnO nanorods prepared using, 0.01 M revealed better surface coverage, the shape of nanorods on this figure is more uniform for all ZnO nanorods.

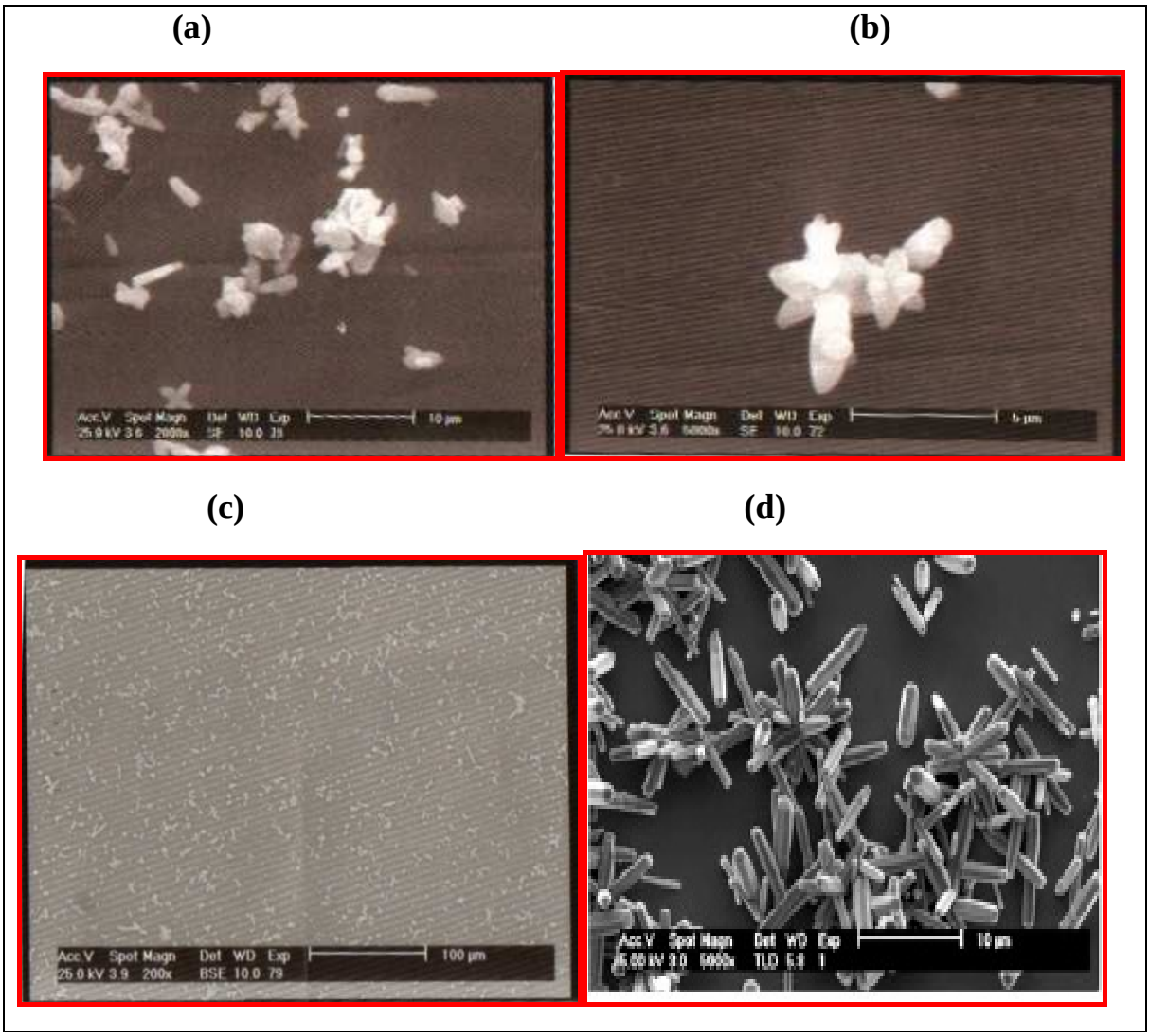

***Figure 5.3**: Randomly orientated ZnO nanorods which were deposited hydrothermally on Si<100> substrates without any pre-coating, (a) ZnO nanorods which were prepared at 0.001 M, (b) a magnification showing nanorods growing on top of each other (multipods), (c) shows weak substrate coverage, (d) ZnO nanorods prepared using 0.01M of the HMT+ Zinc nitrate precursor.*

In **Figure 5.4** the concentration of 0.05 M Zinc Chloride was used for all samples. The difference between the samples was the initial PH and the deposition time. **Figure 5.4** (a) and (b) are ZnO nanorods, prepared with an initial PH of 11.2 and deposition time of 4 hours, while figure 28 (c) are ZnO nanorods prepared with an initial PH of 9 and deposition time of 12 hours. From these SEM images it is evident that, samples prepared in a precursor solution with pHi = 11.2, (a) and (b) revealed homogeneous ZnO nanorods structures, while samples prepared from the precursor solution with a PH=9 for 12 hours revealed flower-like morphology. SEM analysis performed on samples where ZnO nanorods were deposited on Si<100> without any pre coating were in agreement with the XRD spectrum in **Figure 5.2** which showed the presence of other peaks besides the c axis [002] planes, proving that nanorods deposited were randomly orientated

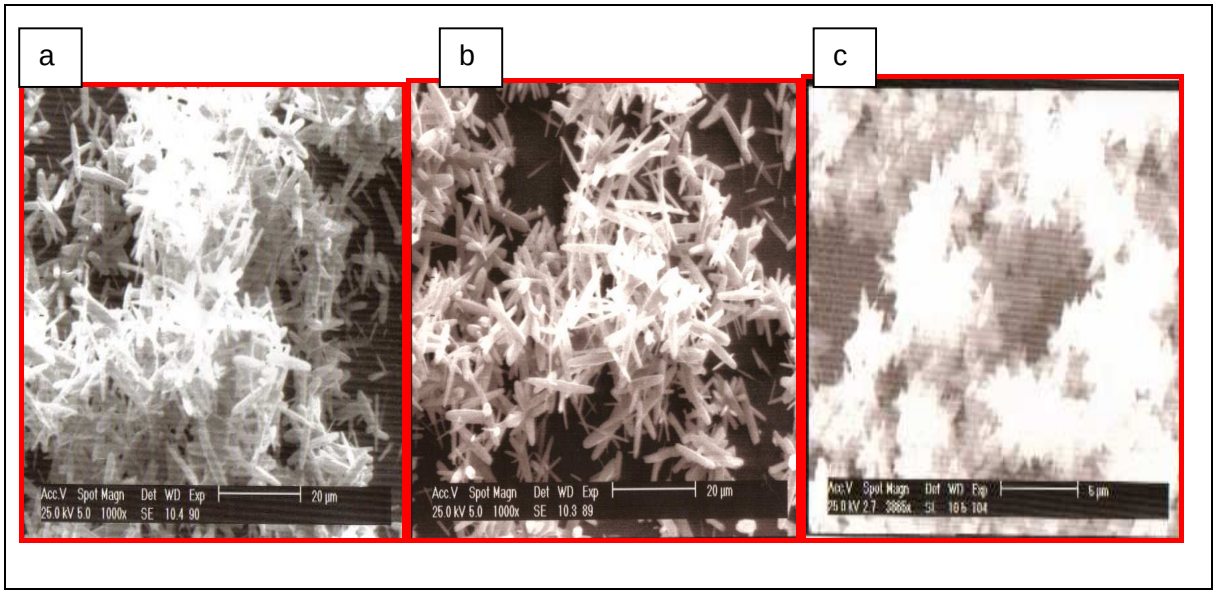

Figure 5.4*: ZnO nanorods prepared with a different initial PH values, (a) and (b) ZnO nanorods prepared with PH=11.2 and (c) ZnO nanorods prepared with PH=9.*

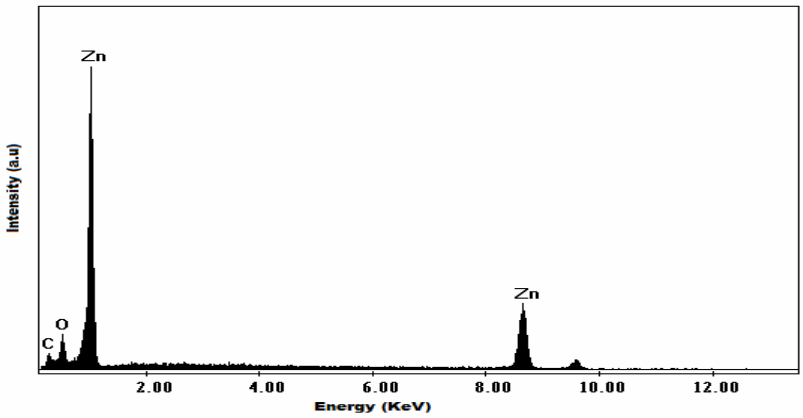

***Figure 5.5**: EDX spectrum of the as-deposited ZnO nanorods*

The EDX analysis performed on the as prepared ZnO nanorods see **Figure 5.5**, showed the presence of zinc and oxygen. No elements used to prepare the precursor solution were present in the EDX spectrum. The presence of carbon was attributed to the double sided carbon tape that was used to mount samples on the SEM stage.

CHAPTER 6

6. ZNO NANORODS SYNTHESIZED ON ZNO SEEDS

6.1. Introduction

This chapter presents results obtained from the ZnO nanorods which were synthesized by hydrothermal synthesis on ZnO thin films deposited by Pulsed laser deposition. The precursor solution for hydrothermal synthesis was prepared using the optimum parameters for Zinc Chloride and aqueous ammonia precursor. The structural and gas sensing properties and the microstructure of the ZnO nanorods were studied using several characterization techniques.

6.2 Experimental

6.2.2 Orientated ZnO Nanorods preparation

Zinc chloride and aqueous ammonia purchased from industrial analytical were used without further treatments. A solution of Zinc Chloride ($ZnCl_2$) with a concentration of 0.05 M was prepared in a 120 ml autoclavable bottle using deionised water as the solvent. To alter the PH aqueous ammonia was slowly added into the $ZnCl_2$ solution under stirring until the PH was 11.2 as this was found to be the best PH value for best substrate coverage if the concentration is 0.05 M.

When the precursor solution was ready, a glass substrate with a ZnO thin film deposited by pulsed laser deposition was immersed vertically into the solution. The precursor solution containing a substrate with a ZnO thin film was then put into an oven at a temperature of 90 ^{o}C for 4 hours as this period was found to yield the best surface coverage for the above mentioned precursor solution parameters. After deposition samples were removed and cleaned with deionised water to remove salts and amino complexes precipitated during deposition and dried in air.

6.3 Results and discussions

6.3.1 X-Ray Diffraction

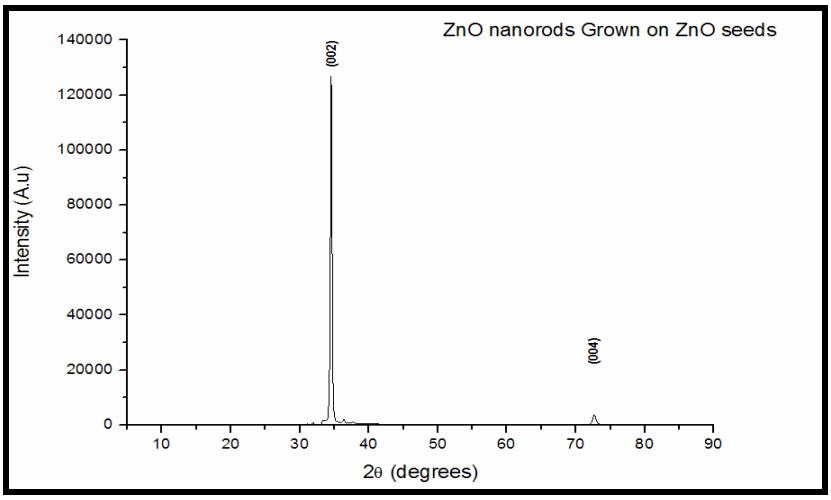

***Figure 6.1**: The XRD pattern of orientated ZnO nanorods*

The XRD pattern of ZnO nanorods deposited on ZnO seeds showed greater orientation along the C-axis (002), see **Figure 6.4**. The high intensity of planes along the c-axis proved that the ZnO

nanorods deposited were along the c-axis and were perpendicular to the substrate. All samples where ZnO nanorods were deposited on ZnO seeds showed similar characteristics.

6.3.2 Scanning Electron microscope and EDX

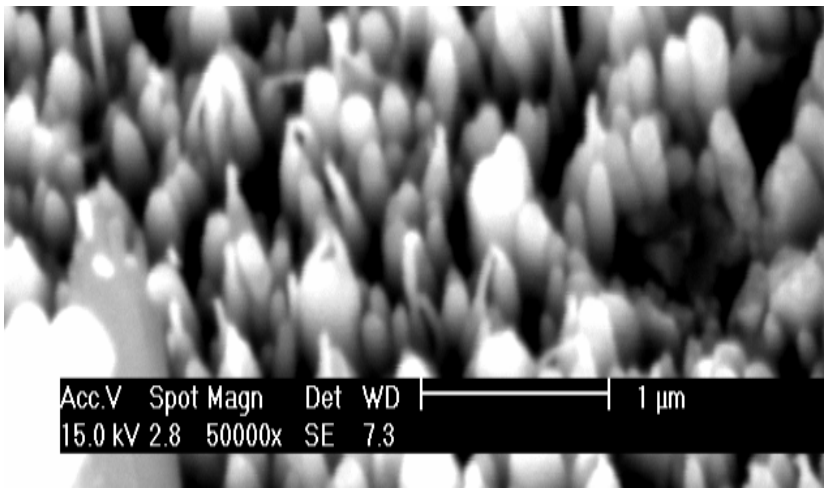

Figure 6.2*: c-Axis orientated ZnO nanorods deposited on a ZnO thin film tilted at an angle of 15* ^{o}.

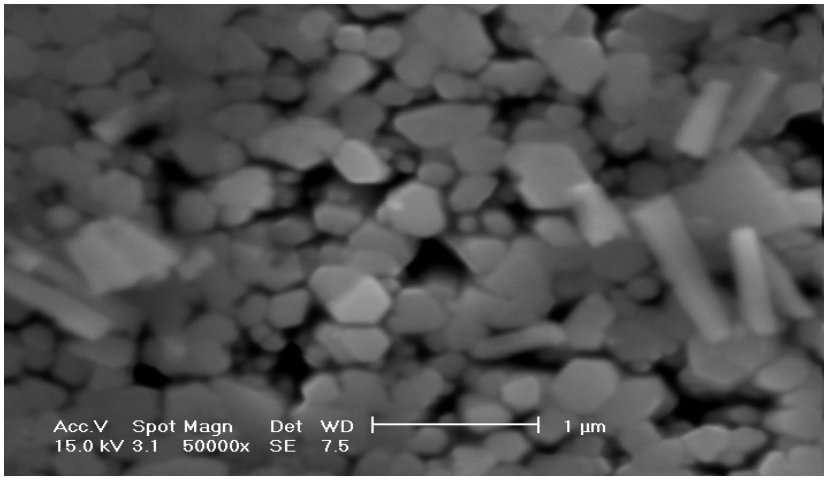

Figure 6.3*: Top view of the as deposited ZnO nanorods on ZnO thin films*

The ZnO nanorods deposited on ZnO thin films using optimum parameters of PH and concentration for zinc chloride and aqueous ammonia showed good surface coverage on the thin film. The sample used in **Figure 6.2** was deposited on the substrate with ZnO seeds (thin-films with a thickness of 13 µm). The ZnO nanorods on **Figure 6.2 and 6.3** were orientated along the c-axis and perpendicular to the substrate, as shown by the XRD pattern in **Figure 6.1**. The as deposited ZnO nanorods had a diameter and length range of 100-250 nm and 500-800 nm respectively.

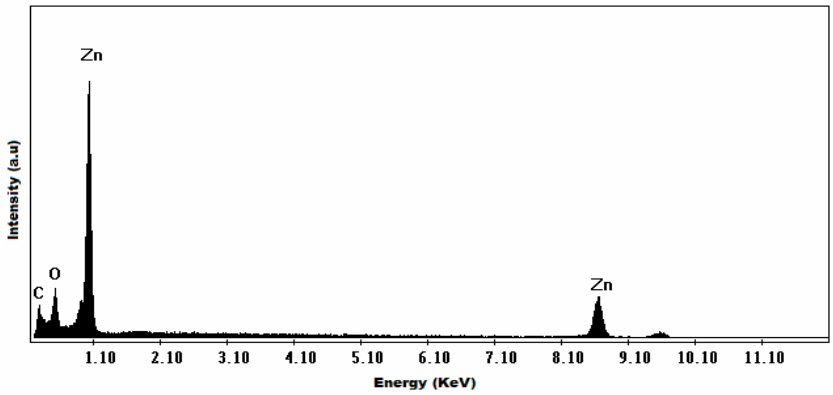

Figure 6.4: *EDX spectrum of the as-deposited orientated ZnO nanorods*

The EDX analysis done on the sample with oriented ZnO nanorods, see **Figure 6.4** did not show any presence of impurity elements found in compounds which were used to prepare precursor solutions. This proved that the as-deposited ZnO nanorods were perfect stochiometric ZnO. The presence of carbon was attributed to double sided carbon tape used for sample mounting.

6.3.3 Gas sensing properties

ZnO thin-films with ZnO nanorods were found to have more resistance in air when compared to ZnO thin films at similar temperatures. This was found to be the possible reason contributing to their superior sensitivity to test gases when compared to ZnO thin-films without ZnO nanorods, as these high resistance values dropped exponentially with an increase in temperature and the introduction of the test gas.

6.3.3.1 Hydrogen sensing for Orientated ZnO nanorod arrays

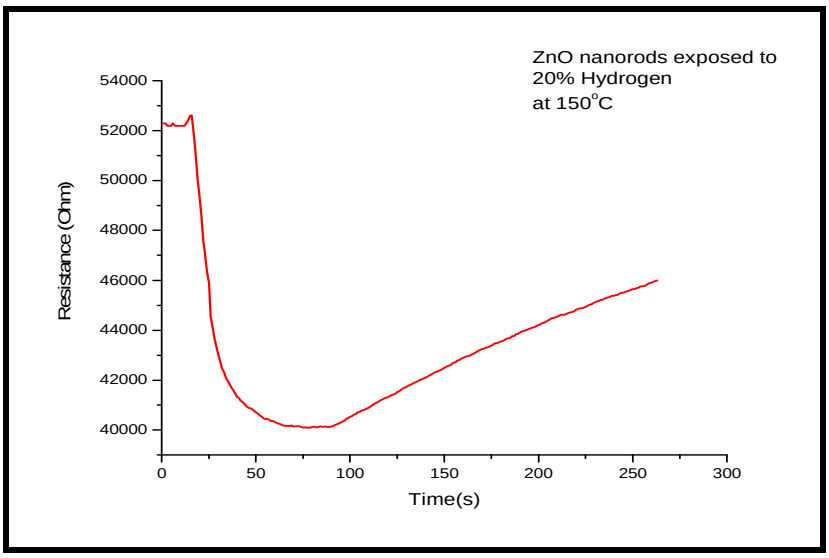

***Figure 6.5**: Orientated ZnO nanorods exposed to hydrogen at 150°C*

When a sample with orientated ZnO nanorods was exposed to hydrogen at 150 °C, as shown in F**igure 6.5**, the response time for the gas sensor was found to be 17 seconds, which is the period for sharp resistance decrease before stabilization. The resistance of this sample decreased from 52600 Ω to 40100 Ω, the sensitivity was therefore 23%. The ZnO nanorods based gas sensing

film was found to experience permanent reduction at this temperature; this was confirmed by the poor recovery of the sensor to return to its original resistance. The sensor took 171 seconds to recovery 86 % of its original resistance (resistance in air).

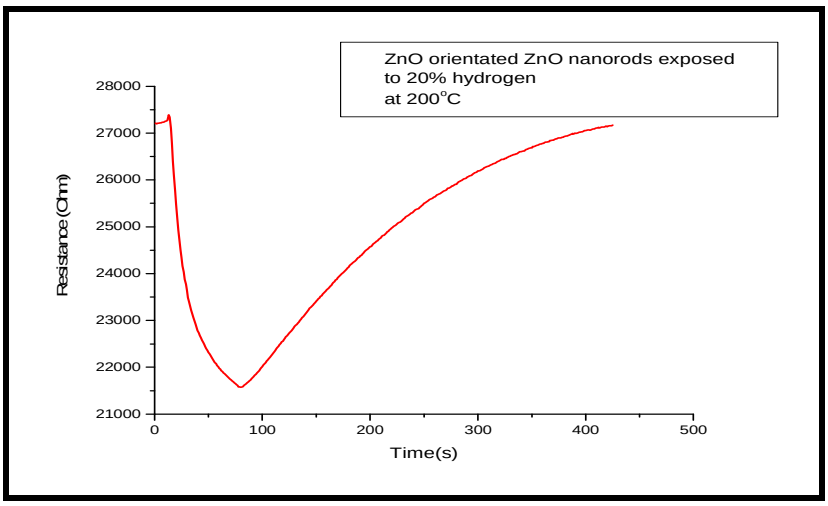

***Figure 6.6**: Orientated ZnO nanorods exposed to hydrogen at 200°C*

At 200 °C the response time of the ZnO nanorods containing sample was found to be 18 seconds, see **Figure 6.6**. The resistance of the sample at this temperature, decreased from 27340 Ω to 21580 Ω. The sensitivity at this temperature was calculated to be 27% .The recovery time at this temperature was found to be 290 seconds for 100 % recovery. From this it can be seen that the ZnO nanorods based gas sensor does not experience permanent reduction at 200°C.

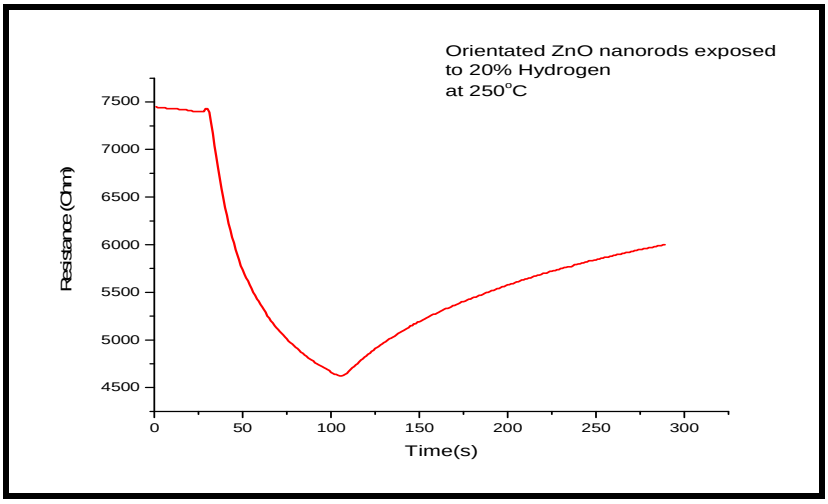

***Figure 6.7**: Orientated ZnO nanorods exposed to hydrogen at 250°C*

When the ZnO nanorods based sample was exposed to hydrogen at 250 °C, see **Figure 6.7**, the response time was found to be 20 seconds. The resistance of the sample decreased from 7430 Ω to 4762 Ω and the sensitivity was 37%. However at this temperature the film sensor experienced a permanent reduction of its original resistance. This was further confirmed by the period of recovery for the sample's resistance at this particular temperature. The sensor took 177 seconds to recover about 75% of the original resistance.

The response time of the ZnO nanorods based gas sensing sample when exposed to hydrogen was found to be 10 s, at 350 °C, see **Figure 6.8**. At this temperature the resistance of the sensor decreased from 1150 Ω to 440.9 Ω and the sensitivity was 70%. The sensor was found to experience permanent reduction at this temperature since it does not fully recover to it original resistance. The sensor recovered up to 61% of it resistance in air this recovery took, 113 s.

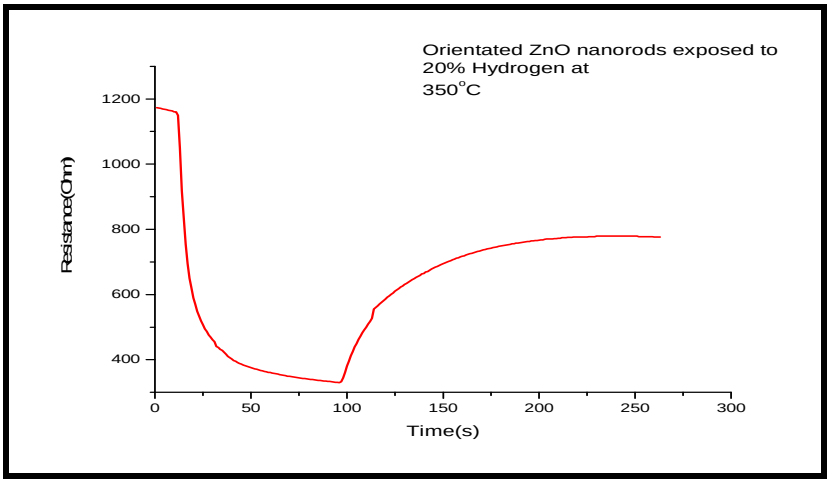

***Figure 6.8**: Orientated ZnO nanorods exposed to hydrogen at 350°C*

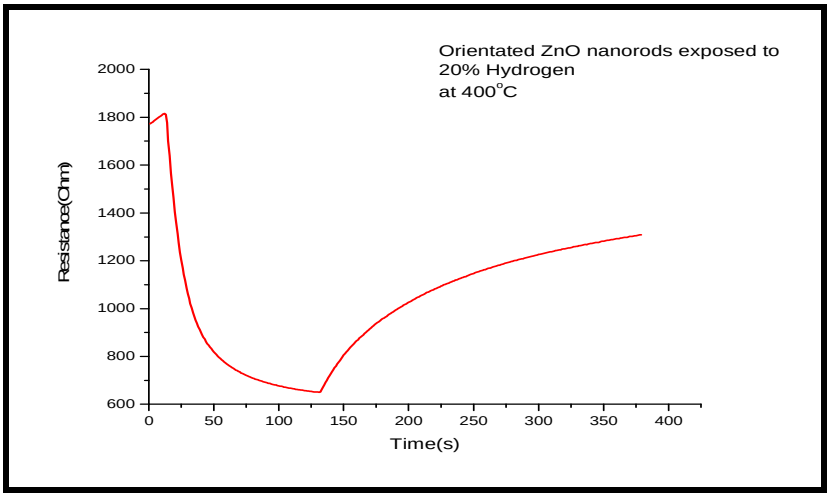

***Figure 6.9:** Orientated ZnO nanorods exposed to hydrogen at 400°C*

The response time at 400 °C, see **Figure 6.9** was found to be 34 seconds, and the resistance decreased from 1812 Ω to 796 Ω and the sensitivity was 62%. The sensor also experienced permanent reduction at this temperature as it took 178 seconds to only recover 68 % of it original resistance.

The sensitivity of the ZnO nanorods based sample was at it optimum at 350 ^{o}C see, **Figure 6.10**. At this temperature the sensitivity (%) was found to be 70%. However at this temperature the sensor experienced permanent reduction which caused it to recover only 80 % of it original resistance. The only temperature which caused the sensor to fully recover after hydrogen reduction was 200^{o}C, however this temperature had sensitivity (%) of only 27%, thus the sensor could only function well at 350^{o}C. The growth of orientated ZnO nanorods onto ZnO thin films improved the gas sensitivity of the gas sensor by increasing the resistance of the sensor and the surface area to volume ratio. For the thin film sensor the maximum sensitivity (%) was found to be 69% and was found to exist at 400^{o}C. The introduction of ZnO nanorods caused a maximum sensitivity of 70% at 350 ^{o}C, thus ZnO nanorods based samples were more sensitive at a lower temperature, when compared to thin films.

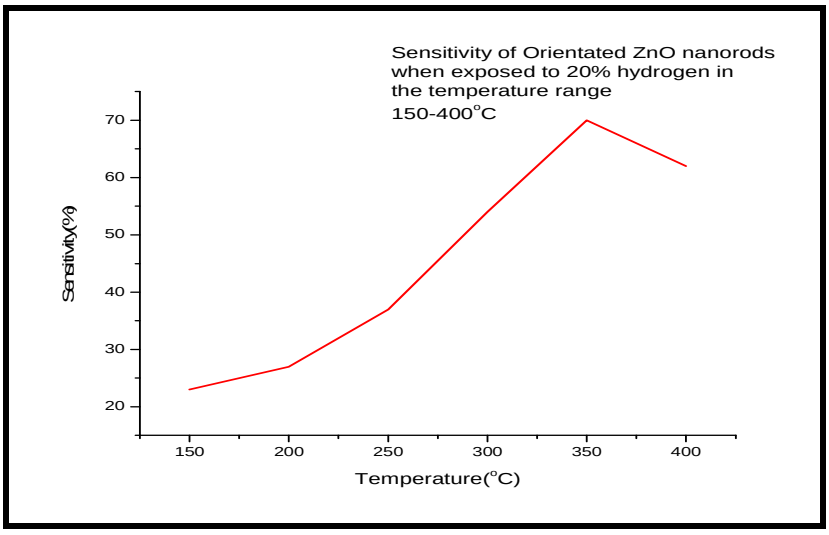

***Figure 6.10**: Sensitivity of ZnO nanorods exposed to hydrogen at different temperatures.*

6.3.3.2 Acetylene Sensing Orientated ZnO nanorod arrays

After the introduction of orientated ZnO nanorod arrays on ZnO thin films, the minimum temperature at which the sensor started to sense acetylene was reduced to 300 ^{o}C compared to that of ZnO thin films without Orientated ZnO nanorods

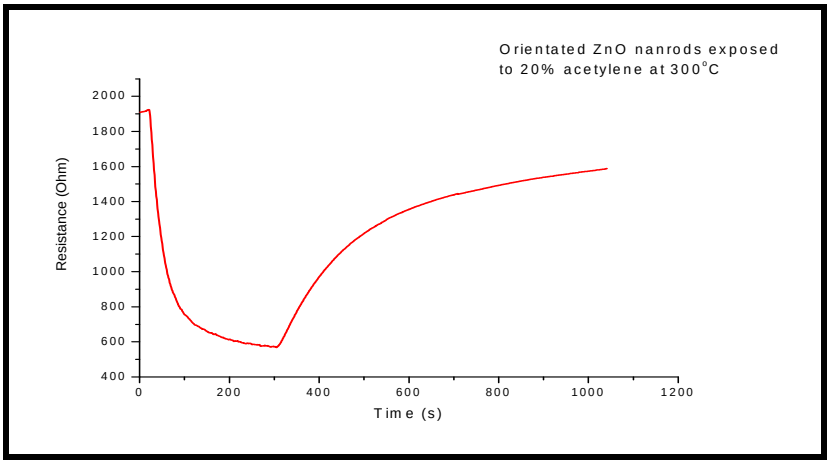

***Figure 6.11**: Orientated ZnO nanorods exposed to 20 vol% acetylene at 300^{o}C.*

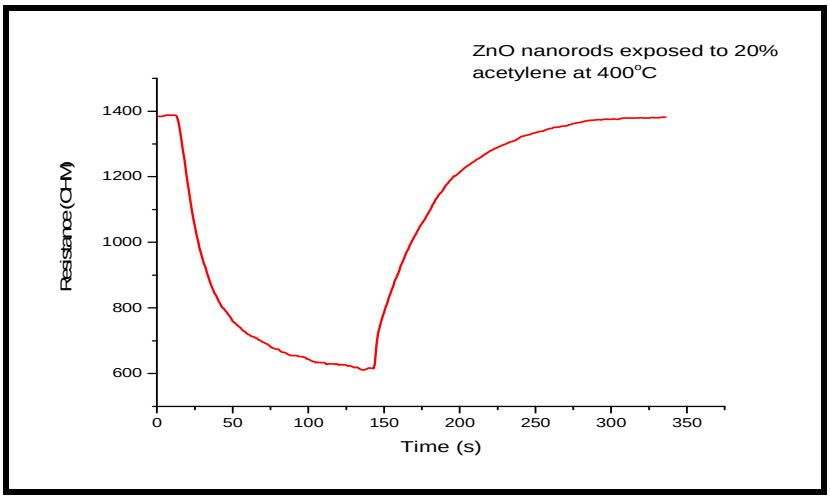

***Figure 6.12**: Change of resistance with respect to time as 20% flow of acetylene was introduced into the chamber with nitrogen as the carrier gas.*

The response time of sample containing orientated ZnO nanorods, see **Figure 6.11** was 12 seconds when it was exposed to 20% acetylene at 300 ^{o}C. The sensor showed a more stable behaviour at this temperature. There were no sharp jumps in resistance. This was due to the fact that at higher temperatures there are more adsorption sites on the surface of the ZnO thin film and nanorods for the oxidation atomic hydrogen.

CHAPTER 7

7. ORIENTATED ZNO NANORODS DOPED WITH PB

7.1 Introduction

This chapter presents results obtained from Lead (Pb) doped ZnO nanorods which were synthesized by hydrothermally on ZnO seeds deposited by Pulsed laser deposition. The precursor solution for hydrothermal synthesis was prepared using $Zn(NO_3)_2$ and HMT, $Pb(NO_3)_2$ Lead (II) nitrate was used as the source of Pb for doping. The characterization was carried out using the Scanning Electron Microscope equipped with EDX, XRD and Tru RMS multimeter.

7.2 Experimental

7.2.1 Orientated Pb Doped ZnO nanorods preparation

An equimolar concentration of 0.01 M for Zn $(NO_3)_2$ and HMT was used to prepare a precursor solution using deionised water as a solvent and a 120 ml autoclavable as a reactor vessel. For the Lead (II) source 0.001 M of Lead (ii) nitrate (Pb $(NO_3)_2$) was added into the precursor solution. ZnO seeded substrates were then immersed vertically into the prepared solutions. The growth period and temperature were set at 18 h and 90^{o}C respectively as this deposition time was discovered to yield the best substrate coverage for this precursor solution. After the synthesis of

Pb doped ZnO nanorods, the samples were removed from the solution and rinsed with deionised water and dried at room temperature.

Ag contacts were deposited using the Edwards vacuum coater. Ag was placed on Tungsten boat. The middle section of the ZnO thin-film was covered with a glass and placed face down on the sample holder. The pressure of the deposition chamber was pumped down until it was better than 4 x 10^{-6} mbar. Deposition was carried out for 20 seconds. The vacuum coater was allowed to cool down and the sample was removed.

7.3 Results and discussions

7.3.1 X-ray diffraction

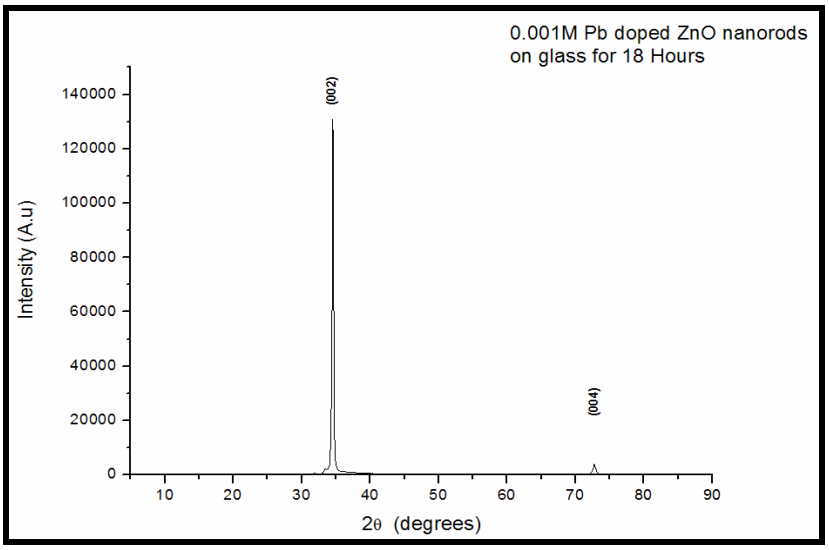

***Figure 7.1**: XRD pattern of orientated ZnO nanorods arrays, which were doped with 0.001M of Pb.*

The high intensity of the (002) planes and the absence of other intensity peaks suggested that the Pb-doped ZnO nanorods deposited on ZnO seeds (thin films) were orientated along the c-axis and perpendicular to the substrate, see **Figure 7.1**. Chu et al. **[31]** showed that Pb^{2+} ions replace Zn^{2+} ions in the ZnO wurtzite crystal structure. The recorded increase in interplanar spacing of doped ZnO nanorods when compared to virgin ZnO was caused by the introduction of Pb^{2+} which has a longer atomic radius than Zn^{2+}. From these findings it was evident Zn^{2+} atoms were replaced by Pb^{2+} atoms when ZnO nanrods were doped hydrothermally using $Zn(NO_3)_2$ + HMT and $Pb(NO_3)_2$ as the source of Pb^{2+} for atoms.

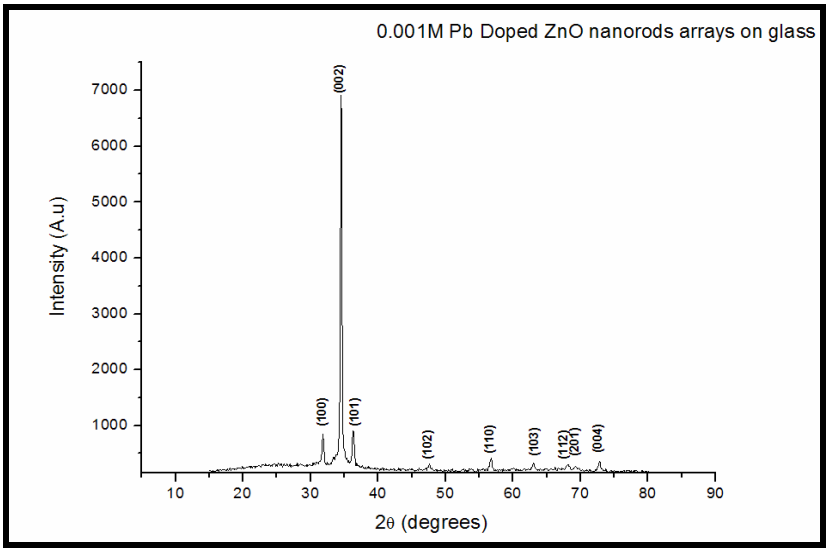

***Figure 7.2**: XRD pattern of Pb doped ZnO nanorods deposited on glass for 18 hours.*

Pb doped ZnO nanorods deposited on glass were expected to orientate themselves randomly because of the absence of seeds. The XRD pattern, see **Figure 7.2** confirmed this with the presence of other peaks other than the (002) planes which are planes along the c-axis.

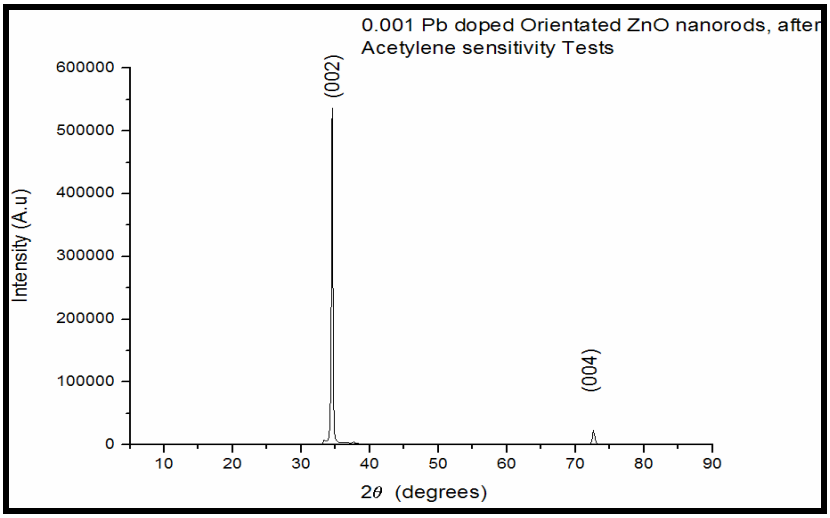

***Figure 7.3**: XRD pattern of Pd doped oriented ZnO nanorods after acetylene sensitivity tests were performed.*

After acetylene tests were performed, the sample used for tests was analysed using XRD. The XRD pattern given in **Figure 7.3** showed that although acetylene contains carbon, the sample used was not contaminated by carbon. The wurtzite crystal structure of the sample was also not affected, with (002) planes being the most dominant plane orientation before and after use, proving that the sample was not affected by exposure to the test gases and elevated temperatures. There were no new peaks observed.

7.3.2 Scanning Electron Microscope and EDX

The Pb doped ZnO nanorods deposited on ZnO thin films were also found to be perpendicular to the substrate, see **Figure 7.4**. The diameter range of doped ZnO nanorods was 100-250 nm, length range was 500-800 nm. When Pb doped ZnO nanorods were deposited, for extended periods, microrods started to form on top of the orientated ZnO nanorods see **Figure 7.5.**

(a)

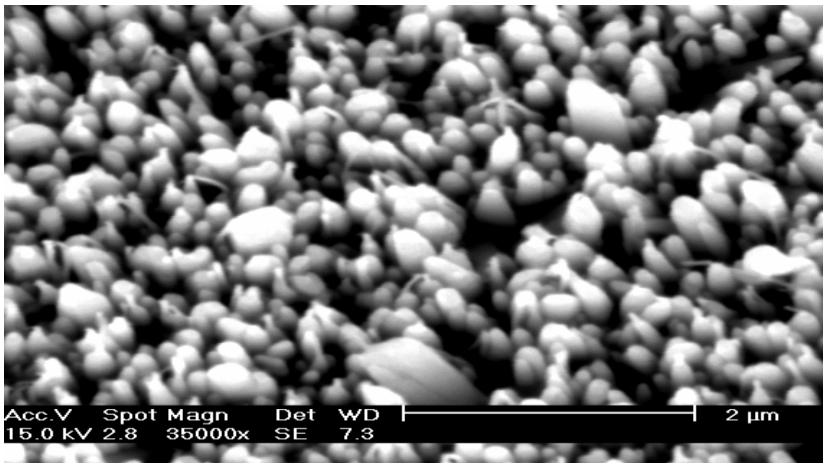

(b)

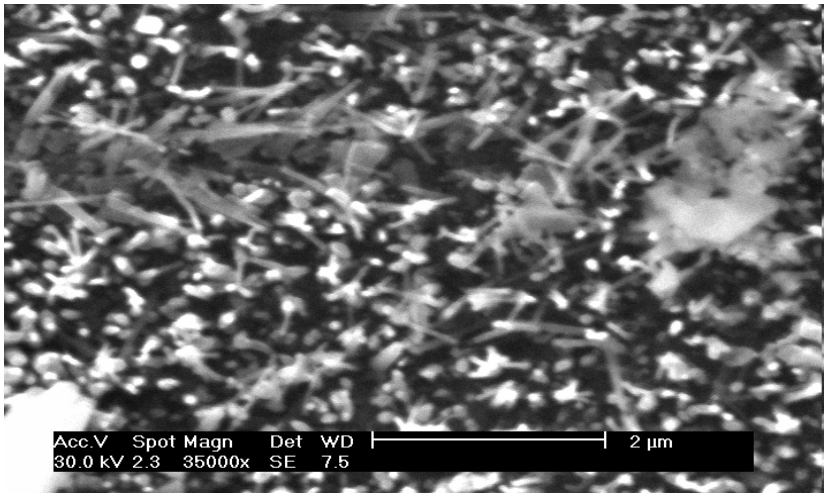

***Figure 7.4**: Orientated ZnO nanorods doped with Pb*

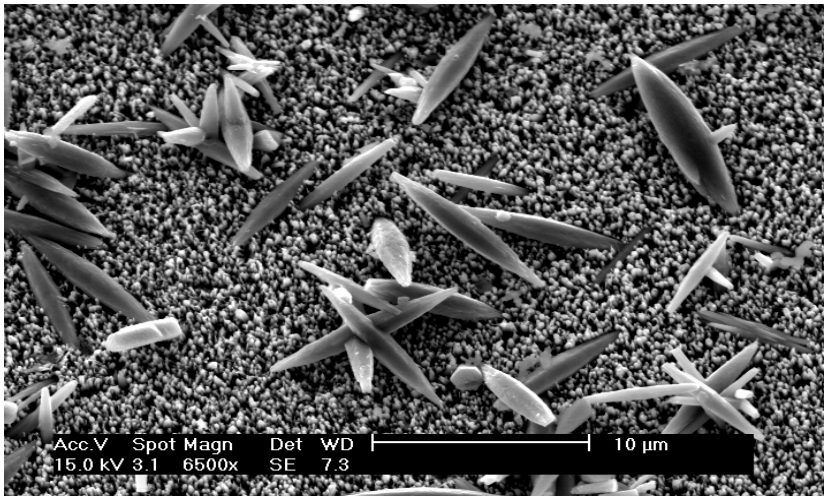

Figure 7.5*: Pb doped ZnO nanorods, which were deposited on top of a ZnO thin film for an extended period of time (24 hours).*

The XRD pattern showed perfect orientation along the c-axis for Pb doped ZnO nanorods deposited on ZnO seeds. The top view SEM images of these samples seen in **Figure 7.3 and 7.4** proved the c-axis as the preferred orientation of growth with most nanorods growing perpendicular to the substrate.

The EDX analysis performed on these samples; see **Figure 7.6,** showed the presence of Pb. The intensity of Pb compared to oxygen and zinc was very small proving that Pb was used as a dopant. The EDX spectrum did not show any impurity elements which were used for preparing the precursor solution. The absence of these elements showed that all reagents reacted to form Pb doped ZnO nanorods

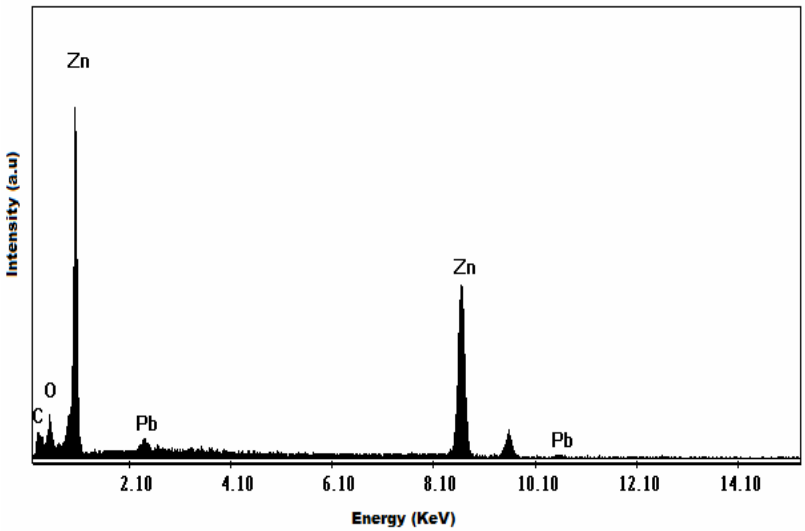

***Figure 7.6**: The EDX spectrum of the Pb doped ZnO nanorods deposited on ZnO seeds*

7.3.3 Gas sensing properties

When compared to ZnO thin-films and virgin orientated ZnO nanorods, Pb doped ZnO nanorods were found to have more resistance in air at similar temperatures. Doped ZnO nanorods samples having this property were also found to have the best sensitivity when compared to other samples. Like ZnO nanorods the values of resistance dropped drastically, when these Pd-doped ZnO nanorods were exposed to test gases yielding superior sensitivity.

7.3.3.1 Hydrogen gas sensing of Pb doped orientated ZnO nanorods arrays.

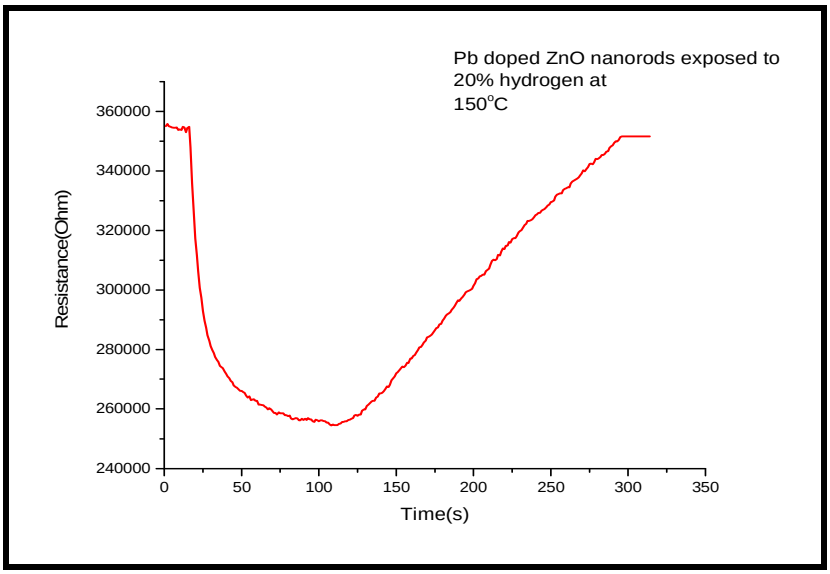

***Figure 7.7**: Pb doped ZnO nanorods exposed to 20% hydrogen at 150 ^{o}C*

At 150 ^{o}C, the response time of the sample was found to be 14 seconds. The resistance of the sensor decreased from 354900 Ω to 254800 Ω; as a result the sensitivity was 28 %. The recovery period of the sample was 188 seconds at this temperature.

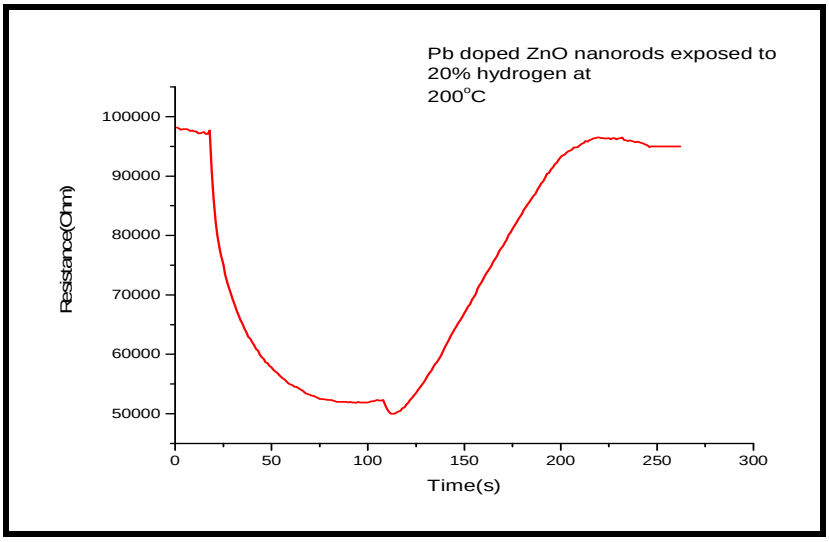

***Figure 7.8**: Pb doped ZnO nanorods exposed to hydrogen at 200 °C*

At 200 °C, see **Figure 7.8,** the response time of the sample was found to be 21 s. The resistance of the sample decreased from 97700 Ω to 52400 Ω. The sensitivity of the sample at this temperature was 46 % with a recovery time of 112 seconds.

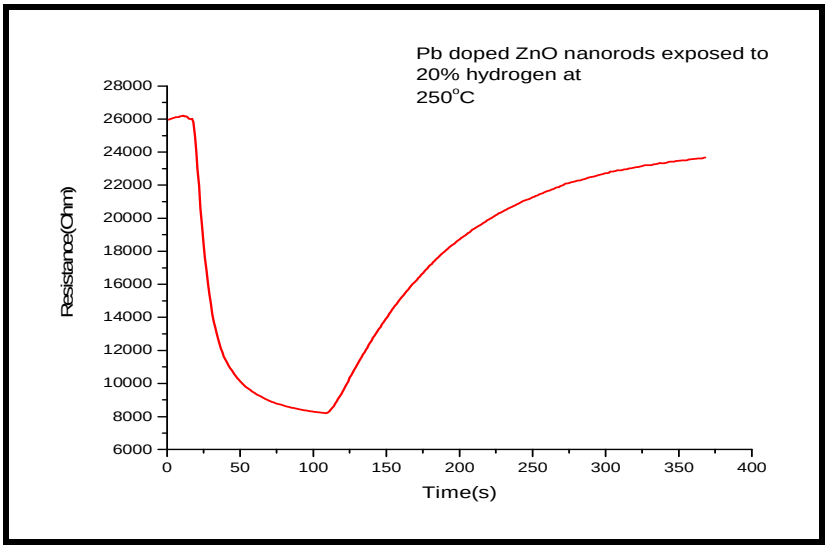

***Figure 7.9**:Pb doped ZnO nanorods exposed to hydrogen at 250 °C*

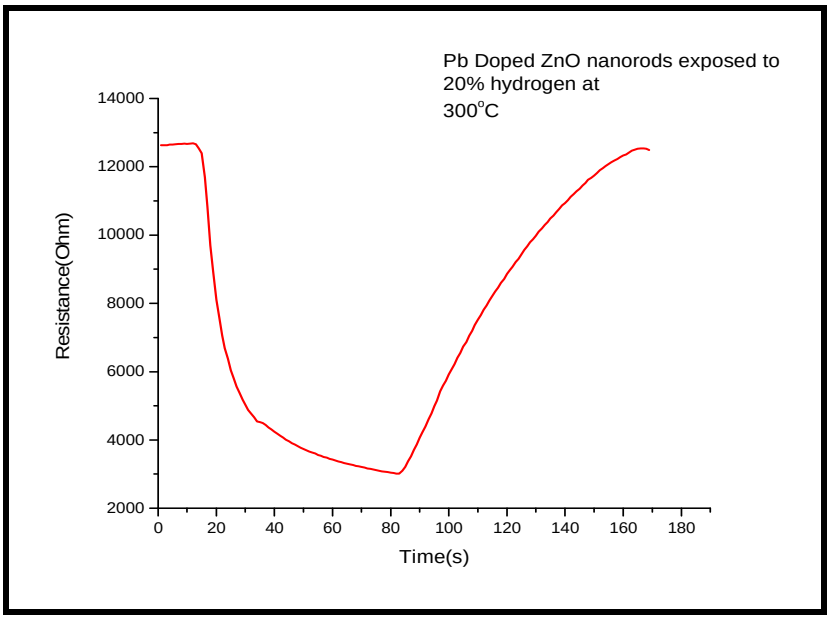

***Figure 7.10**: Pb doped ZnO nanorods exposed to hydrogen at 300 ^{o}C*

The Pb doped ZnO nanorods sample had a response time of 14 seconds at 250 ^{o}C, see **Figure 7.9.** The resistance of the sensor decreased from 25820 to 8380 Ω, as a result the sensitivity of the sensor was 67 %. The recovery time of the sensor was 189 seconds.

At 300 ^{o}C the sensor had a response time of 12 seconds, see **Figure 7.10.** The resistance of the sensor decreased from 12660 Ω to 3151 Ω. The sensitivity was found to be 75 % at this temperature. The recovery time of the sensor was 76 seconds.

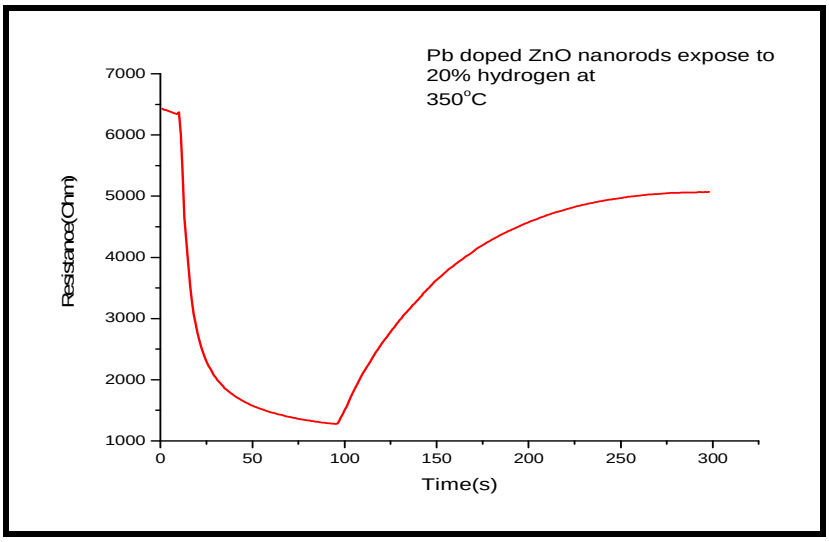

***Figure 7.11**: Pb doped ZnO nanorods exposed to hydrogen at 350 ^{o}C*

The response time of 9 seconds was achieved at 350 ^{o}C. At this temperature the resistance decreased from 6370 to 1345 Ω, see **Figure 7.11**. The recovery time of the sample at this temperature was, about 139 seconds. The sensitivity of the sensor was 78%.

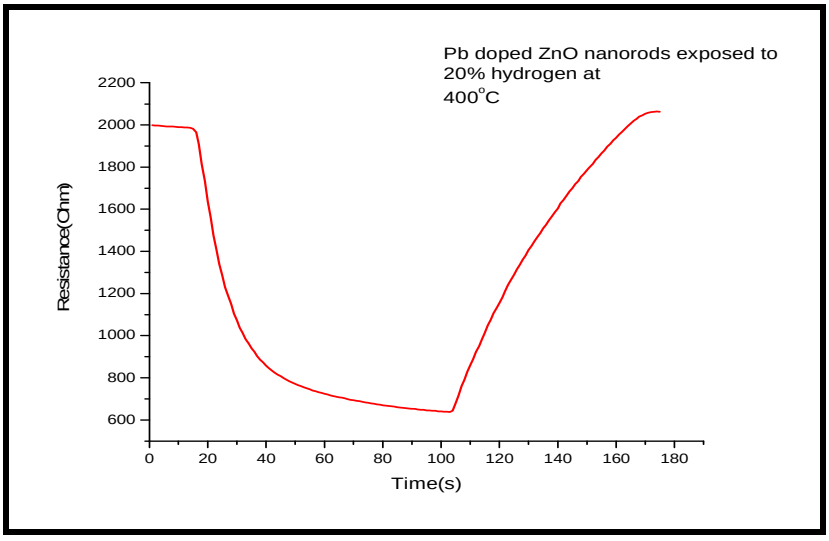

***Figure 7.12**: Pb doped ZnO nanorods exposed to hydrogen at 400 ^{o}C*

At 400^{o}C the sensitivity of the sample was found to be 66%. The response and recovery time of the sensor at this temperature were respectively 16 and 63 seconds. The resistance of the sensor decreased from 1965 to 668 Ω, see **Figure 7.12**

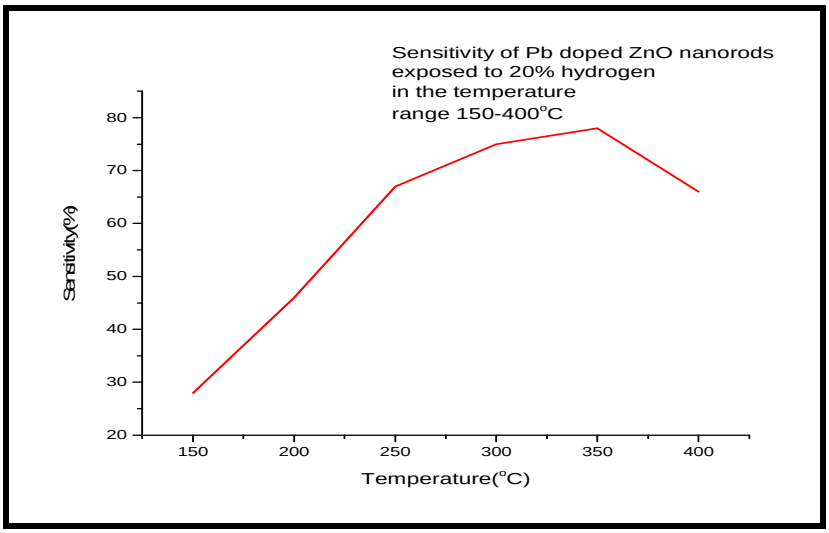

***Figure 7.13**: Sensitivity of Pb doped ZnO nanorods at different temperatures for hydrogen*

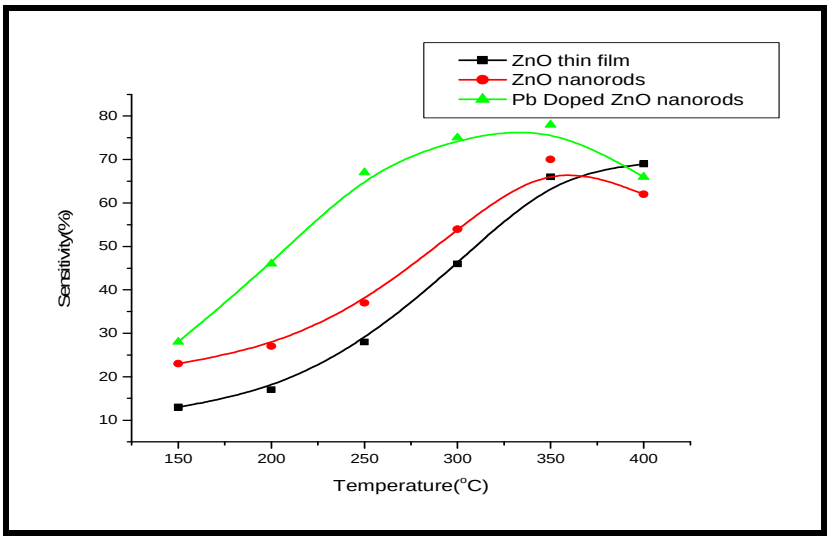

***Figure 7.14**: Comparison of sensitivity between, ZnO thin film, ZnO nanorods and Pb doped ZnO nanorods in temperature range 150-400 ^{o}C.*

From, **Figure 7.14**, it can be seen that by introducing ZnO nanorods on a ZnO thin film, a gas sensor with improved sensitivity at low temperatures is achievable. This was supported by the fact that ZnO nanorods were found to have improved sensitivity at lower temperature than thin films. ZnO nanorods samples were found to have more resistance than ZnO thin films without ZnO nanorods. When Pb was introduced as a dopant into ZnO nanorods, the sensitivity of the doped ZnO nanorods improved. The resistance of the sample with Pb doped ZnO nanorods was more when compared to both, ZnO thin films and undoped ZnO nanorods.

Although the best sensitivity for Pb doped ZnO nanorods is at 350 ^{o}C, the sensitivities and response times of 200 and 250 ^{o}C are good enough for the sensor to also operate in the range between these temperatures.

7.3.3.2 Acetylene gas sensing of Pb doped ZnO nanorods arrays.

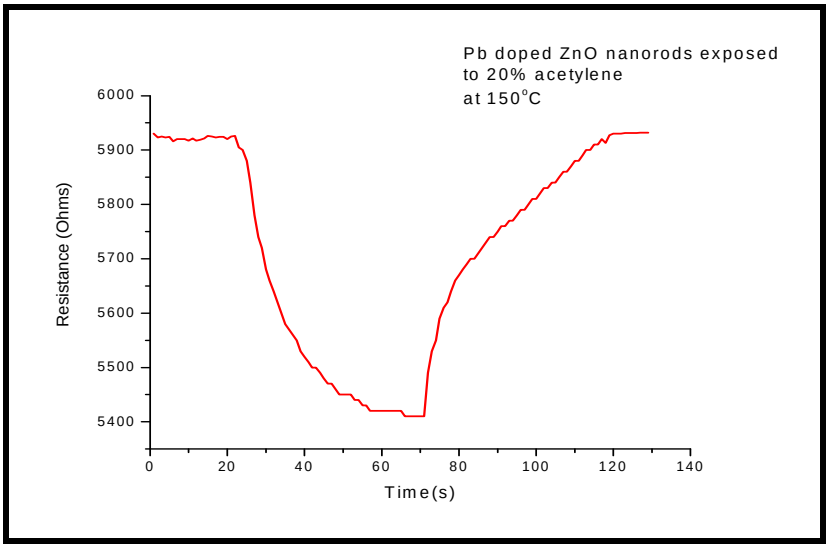

***Figure 7.15**: Pd doped ZnO nanorods arrays, exposed to acetylene at 150 ^{o}C.*

Samples with ZnO nanorod arrays doped with Pd were able to sense acetylene at 150 ^{o}C. The response time for Pb doped ZnO nanorod arrays at 150 ^{o}C was found to be approximately 25 seconds, **Figure 7.15**. The resistance of the Pb doped sample decreased from 5.9 to 5.4 k.Ω. The recovery time of the sample was found to be 40 seconds at this temperature for complete recovery, proving that the sensing layer of the sample is not permanently reduced by exposure to acetylene at 150 ^{o}C.

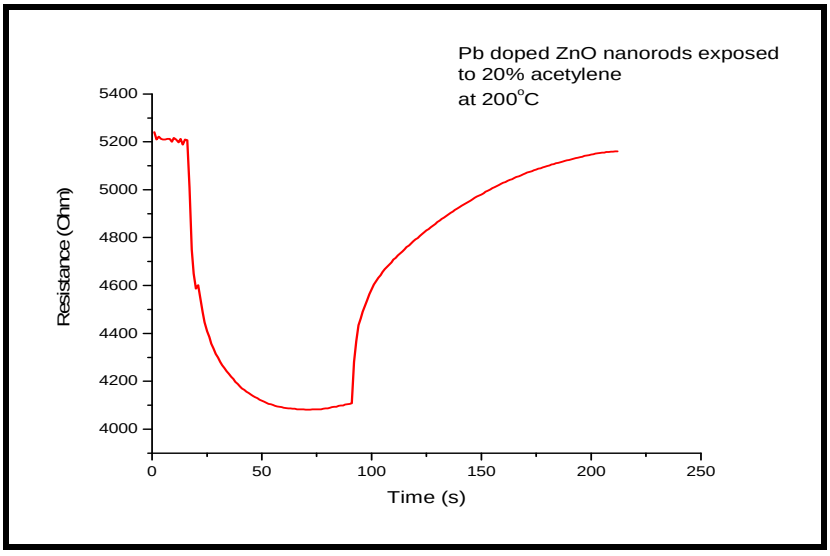

***Figure 7.16**: Pb doped ZnO nanorod arrays at a temperature of 200 ^{o}C when they are exposed to acetylene.*

When Pb doped ZnO nanorod arrays were exposed to acetylene at 200 ^{o}C the resistance of the sensor decreased from 5200 Ω to 4100 Ω, **Figure 7.16**. Compared to the same Pb doped ZnO nanorods at 150 ^{o}C, there was an improvement on the difference in resistance between the

resistance of sensor in air and the resistance of the sensor that is exposed to acetylene. This difference in resistance of about 1100 Ω was achieved in 15 seconds. Compared to 150 ^{o}C, the sensor at 200 ^{o}C had a better response time of 15 s.

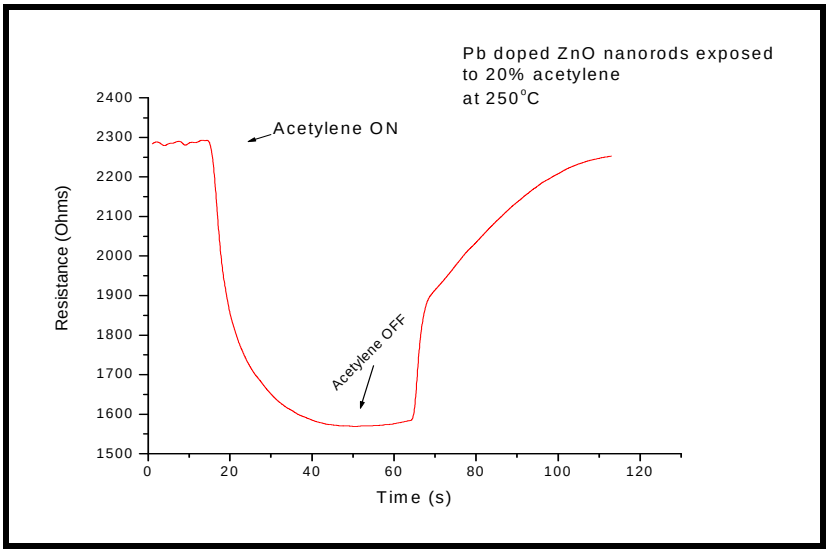

***Figure 7.17**: Pb doped ZnO nanorod arrays at 250 ^{o}C when they are exposed to acetylene.*

When Pb doped ZnO nanorods were exposed to acetylene at 250 ^{o}C, the resistance of the Pd doped sample decreased from 2300 Ω to 1650 Ω, **see Figure 7.17**. After that the resistance started to stabilise, until the minimum resistance of about 1570 Ω was reached. In the region of sharp decrease the resistance of the sensor took 13.5 seconds to reach it minimum before the stabilization stage.

At 250 ^{o}C the recovery time of the Pb doped gas sensing sample was found to be 35 seconds. Because Acetylene is highly flammable and the minimum temperature that can cause it to

explode is 335 ^{o}C to 3 % acetylene. The temperature of 250 ^{o}C was found to be ideal for Pb doped ZnO nanorods, as it was found to exhibit better response and recovery time.

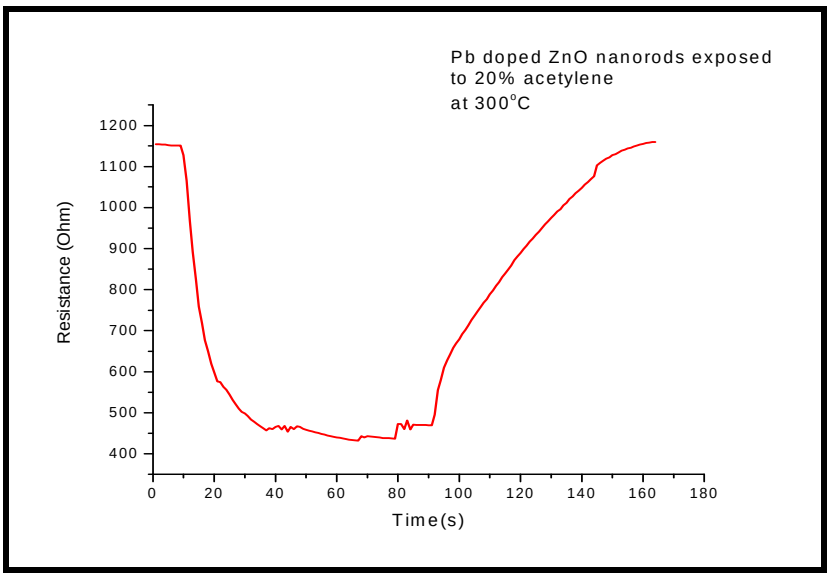

***Figure 7.18**: ZnO nanorods doped with Pb when they are exposed to acetylene at 300 ^{o}C.*

When Pd doped ZnO nanorods were exposed to acetylene at 300 ^{o}C, with an initial resistance of 1150 Ω, the resistance of the sensor dropped to 520 Ω in 13 seconds then after that period, it started to stabilise. The area of interest for the fabrication of a good gas sensor is the area of sharp decrease. Although the difference between the initial and final resistance was found to be smaller at 300 ^{o}C than lower temperatures, the response time was better.

Pb doped ZnO nanorods at 300 ^{o}C showed better response time compared to lower temperatures, however the recovery time for the gas sensor was 60 seconds, when compared to 250 ^{o}C, this is 25 seconds longer, thus the behaviour of Pd doped ZnO nanorods was deemed optimal at 250 ^{o}C.

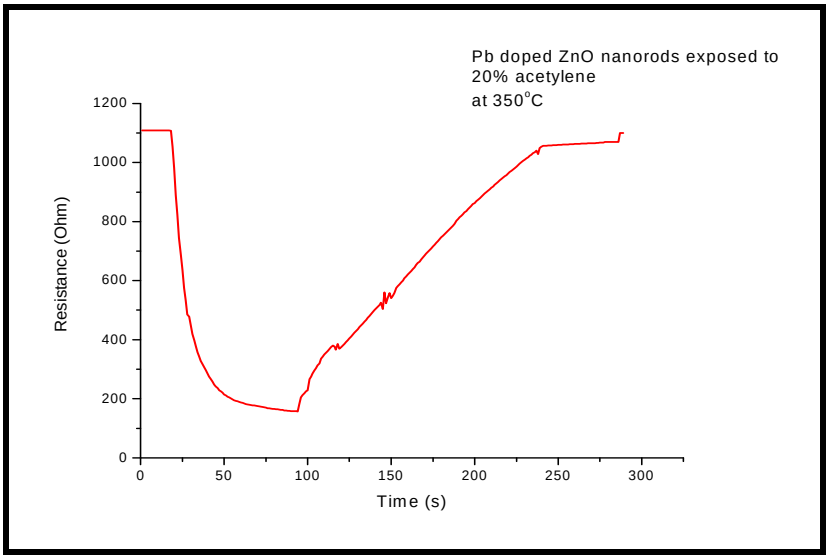

***Figure 7.19**: ZnO nanorods doped with Pb when they are exposed to acetylene at 350 °C.*

At 350 °C, when exposed to 20% acetylene the resistance of the Pb doped ZnO nanorods decreased from 1107 Ω to 297.4 Ω, **see Figure 7.19**. As a result there was an improvement in sensitivity. However the response time for the sensor at this temperature was found to be 21 s. The recovery time at 350 °C was found to be 144 seconds. The sensitivity was found to be 73% at this temperature.

The response time of Pd doped ZnO nanorods at 400 °C if exposed to 20% acetylene was found to be 53 seconds. The resistance of the Pb doped ZnO nanorod arrays sensor decreased from 836 Ω to 154 Ω. This decrease in resistance means that the sensitivity of the sensor at 400 °C was about 81%.The recovery time of the sensor at this temperature was 459 seconds. At 400 °C the sensor did not fully recover to its initial resistance before the acetylene was introduced.

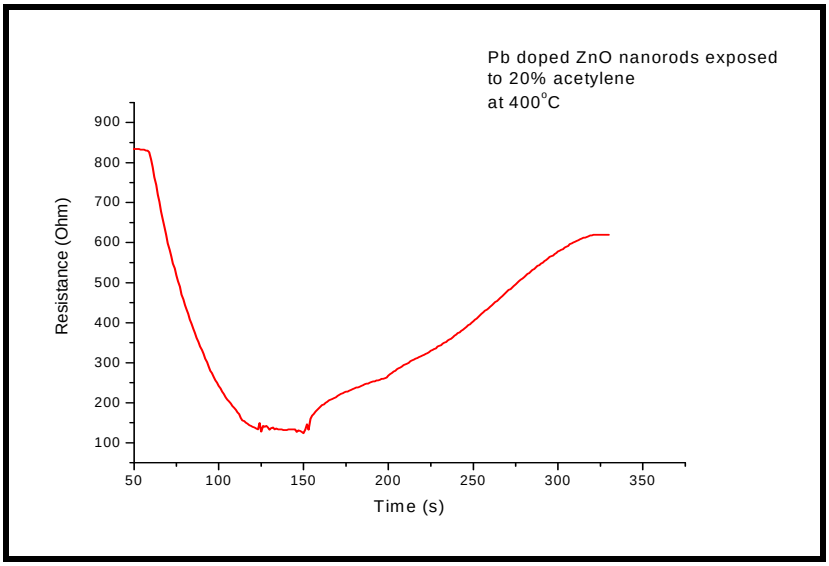

***Figure 7.20**: ZnO nanorods doped with Pb when they are exposed to acetylene at 400 ^{o}C.*

***Table 3**: Pb doped orientated ZnO nanorods when they were exposed to 20% acetylene in the temperature range 150-400^{o}C.*

Temperature (^{o}C)	Response Time (s)	Recovery Time (s)	Sensitivity (%)
150	25	40	8
200	15	77	15
250	13.5	35	23
300	**13**	**53**	**50**
350	**21**	**144**	**73**
400	53	459	81

***Table 4**: Comparison of ZnO thin film sensor, Orientated ZnO nanorods gas sensor and Pb doped ZnO nanorods sensor, when they were exposed to 20% acetylene.*

	SENSOR SENSITIVITY (%)		
Temperature (^{o}C)	**THIN FILM**	**ZnO nanorods**	**Pb Doped Nanorods**
150	-	-	8
200	-	-	15
250	-	-	23
300	-	-	50
350	-	48	73
400	43	50	81

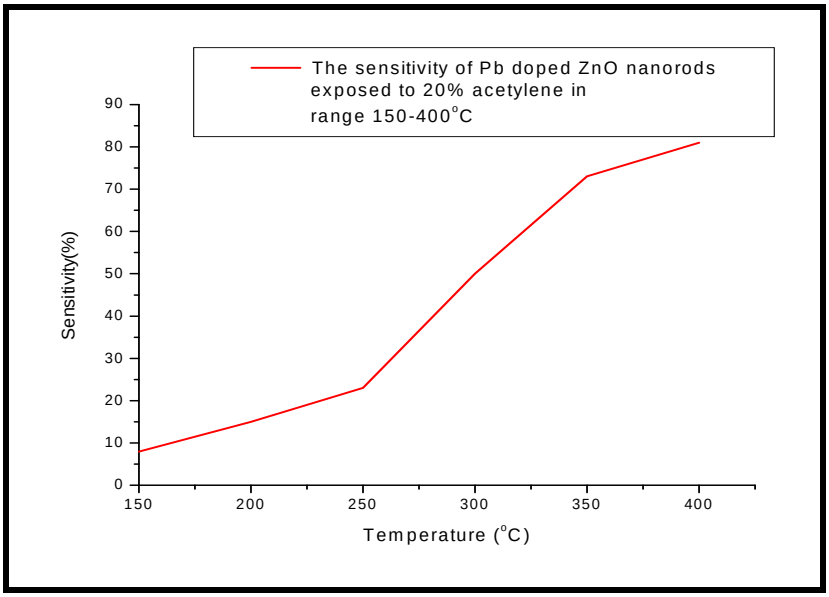

***Figure 7.21**: Sensitivity of Pb doped ZnO nanorods to acetylene as the temperature is increased starting from 150-400^{o}C.*

By doping ZnO nanorods with Pb the sensitivity of the sensor was improved. The Pb sensitized sample was sensitive at 150 ^{o}C, while the ZnO thin film and un-doped ZnO nanorods gas sensor started at 400 ^{o}C and 300 ^{o}C respectively, **Figure 7.21**. The behaviour of the sensor showed that the number of active sites for the oxidation of atomic hydrogen increases exponentially with temperature. The temperature at which the sensitivity of Pd doped ZnO nanorods started to increase sharply was found to be 250 ^{o}C. This temperature is lower compared to un-doped-ZnO nanorods gas sensor. The lower temperature is caused by the catalytic effects of Pb which was used as a dopant. The enhanced sensitivity of Pb-sensitised ZnO nanorods can also be attributed to the formation of highly reactive species according to the equation.

$H_2 + Pb^{2+} = 2H\ (Pb^{2+})$

The atomic hydrogen readily oxidizes according to the equation

$4H\ (Pb^{2+}) + O^{2-} = 2H_2O + e^{-}$

Another possible reason for enhanced sensitivity for Pb-sensitised ZnO nanorods is the increase concentration of O^{2-} at ZnO surface allowing a large number of oxidation centres for atomic Hydrogen, Mitra et al. **[21]** explained the sensitization phenomena for a ZnO thin film sensor doped with Pd^{2+}.

By introducing Pb as a dopant into ZnO nanorods, the optimal temperature range for acetylene gas sensing was established to between 300 and 350 ^{o}C as both of these temperatures have sensitivities higher than 50% and good response and recovery times.

CHAPTER 8

8. SUMMARY AND CONCLUSIONS

8.1 Introduction

Metal oxide based semiconductor gas sensors have attracted great attention over the past few years. The attention they have attracted is due to their low cost and fabrication ease. One of the most studied gas sensing metal oxides is zinc oxide. Zinc oxide nanostructures have also been studied as they have the potential of increasing the surface area to volume ratio for gas sensing. The enhanced surface area to volume ratio potential presented by ZnO nanostructures is likely to result in a gas sensor with enhanced sensitivity at low temperatures. The sensitivity of ZnO nanorods can be improved further by doping with a transition metal element.

This dissertation is a comprehensive study of ZnO thin films, its arrayed ZnO nanorods and Pb doped arrayed ZnO nanorods for hydrogen and acetylene gas sensing applications. It encompasses the deposition of ZnO thin films using Pulsed Laser Deposition, the hydrothermal synthesis of orientated and non-orientated ZnO nanorods, the doping of ZnO nanorods, characterization, device fabrication, and the design of a gas sensing chamber. As a result of this

study, significant gas sensing properties insight has been gained for ZnO thin films, ZnO nanorods and Pb doped ZnO nanorods.

8.2 Summary

This study was divided into five sections namely, 1) the design of the gas sensitivity testing chamber, 2) the study of ZnO thin films deposited using Pulsed laser deposition, 3) the growth of randomly orientated ZnO nanorods on Si <100> wafers, 4) the deposition of orientated ZnO nanorods using ZnO thin films and 5) the deposition of c-axis orientated Pb-doped ZnO nanorods.

In **Chapter 3,** the gas sensitivity testing chamber was designed during this study. The body of the gas chamber/cell was made up of brass. The temperature of the sample was monitored using a thermocouple connected to a multimeter capable of taking temperature readings. The sample stage was made up of 6 resistors connected in parallel. The regulation of all gases inside the chamber was controlled using gas regulators for gases used in this study. The lid of the testing cell had a window to ensure, continuous monitoring of all sample electrical connections during experiments.

For hydrothermal growth of oriented ZnO nanorods doped and un-doped, a pulsed laser deposition system was successfully used to grow highly crystalline ZnO thin films on glass slides. The as-deposited ZnO thin films were found to have uneven ZnO particle sizes, **see**

Chapter 4. The gas sensing characteristics, of the thin films were investigated for hydrogen and acetylene.

Randomly orientated ZnO nanorods on silicon <100> wafers were successfully deposited, **see Chapter 5**. Different precursor concentrations were studied, to establish the concentration that yields the best substrate coverage in the shortest period of time. For the precursor solution made up of zinc nitrate and HMT the optimal equimolar concentration for both reagents was found to be 0.01 M, while for zinc chloride and aqueous ammonia it was 0.05 M and a PH of 11.2.

Orientated ZnO nanorods were successfully growth hydrothermally on glass slides with the as-deposited ZnO thin-films in **Chapter 6** using zinc chloride and aqueous ammonia. The crystal structure of the as-deposited ZnO nanorods was studied using XRD and found to be highly crystalline with strong c-axis orientation. The c-axis orientation was confirmed by studying the as deposited ZnO nanorods with a scanning electron microscope. The EDX did not show any foreign elements on the as-deposited ZnO nanorods. .

ZnO nanorods were doped with Pb by adding Pb $(NO_3)_2$ into the zinc nitrate + HMT precursor solution. The study of Pd-doped ZnO nanorods focused on a single concentration, which was 0.001 M, see **Chapter 7**. The as-deposited nanorods were studied using X-ray diffraction, scanning electron microscope with EDX, and found to be orientated along the c-axis.

8.3 Conclusion

A study of gas sensing characteristics of ZnO thin films, ZnO nanorods and Pb-doped ZnO nanorods was conducted for hydrogen and acetylene. ZnO thin films were deposited on glass using pulsed laser deposition and used for gas sensing and growth of c-axis orientated ZnO nanorods. The optimum concentration and PH values used for orientated ZnO nanorods growth doped and undoped were optimized during depositions performed on Si <100> substrates. Rutherford backscattering, X-Ray diffraction and scanning electron microscope with EDX, were all used to study the thickness, purity and morphology of the as-deposited ZnO thin films and ZnO nanorods. Ag contacts were deposited on all samples using the EDWARDS vacuum coater.

A gas sensitivity testing chamber/ cell was designed during this study. Gas sensitivity studies performed on ZnO thin films deposited by PLD, showed that ZnO thin films started sensing hydrogen at 150^{o}C. However at this temperature the sample did not recover back to it resistance in air value, thus it was concluded that the sample experienced permanent reduction at this temperature when exposed to hydrogen. The optimum operating temperature range was found to be 300-350^{o}C, since this range gave better sensitivity, response and recovery time, when compared to others. The thin film sample could only sense acetylene at 400^{o}C in the temperature range chosen for this study. The response time at this temperature was 30 s. It was thus concluded that a ZnO thin film sensor for sensing acetylene can only operate at 400^{o}C and above, as a result a ZnO thin film acetylene sensitivity graph could not be obtained in the chosen temperature range.

Gas sensitivity tests performed on orientated ZnO nanorods showed that samples with orientated ZnO nanorods had larger resistance in air values when compared to thin films. ZnO nanorods did not recover fully to their resistance in air values, and only recovered at 200^{o}C. It was concluded that ZnO nanorods experienced permanent reduction when exposed to hydrogen. The temperature range which gave the best % Sensitivity was found to be 300-350^{o}C, like ZnO thin films. However ZnO nanorods gave better sensitivity values throughout the temperature range when compared to ZnO thin films. A larger surface area to volume ratio and higher resistance values offered by samples with ZnO nanorods caused them to have better sensitivity when compared to thin films. ZnO nanorods started sensing acetylene at 300^{o}C, slightly lower than thin films; however since they did not sense acetylene in the whole temperature range, thus the sensitivity graph was not obtainable.

Pb-doped ZnO nanorods were found to have the highest resistance in air values when compared to ZnO thin films and pure ZnO nanorods. Unlike ZnO thin films and virgin ZnO nanorods, Pb-doped ZnO nanorods started sensing acetylene at 150^{o}C, proving that doping with Pb improves the sensitivity of ZnO nanorods. Pb-doped ZnO nanorods had a sensitivity of more that 67 % at 250^{o}C. The sensitivity of these Pd doped ZnO nanorods increased up to 78% at 350^{o}C and dropped thereafter. Doping with Pb caused the sensor to be very sensitive at lower temperatures. With Pb doped ZnO nanorods having the highest resistance in air values, followed by pure ZnO nanorods and then thin films. It was concluded that an increase in resistance caused by growing ZnO nanorods on thin films followed by doping them with Pb, caused the sensitivity of the as-deposited nanorods to increase even at low temperatures.

The outcome of this research is better understanding of, 1) ZnO based gas sensors, 2) Hydrothermal synthesis of ZnO nanorods which are orientated along the c-axis of the wurtzite structure, 3) improved understanding of polar-surface-dominated (PSD) phenomena among Wurtzite crystal structures, 4) understanding the effects of the gas bond energy on the optimal functioning temperature of gas sensor and, 5) improved understanding of the effects that doping with Pb has on the sensitivity of ZnO nanorods based gas sensor.

REFERENCES

[1]Wikipedia, the free encyclopedia, " Scanning Electron Microscope", Available online: http://en.wikipedia.org/wiki/Scanning_electron_microscope. (Downloaded:12 March 2007)

[2] Nalwa H.S., (2004). Encyclopedia of Nanoscience and Nanotechnology. **Volume 8**: Pages (147-166)American Scientific publishers.

[3] C.H.Wang, X.F. Chu, M.M.Wu, Detection of H_2S down to ppb levels at room temperature using sensors based on ZnO nanorods, Sensors and Actuators **B 113** (2006) 320–323.

[4] O.Wan, Q.H. Li, J.Y. Chen, H.T.Wang, X.L. He, J.P. Li, C.L. Lin, Fabrication and ethanol sensing characteristics of ZnO nanowire gas sensors, Applied Physics Letter **84** (2004) 3654–3656.

[5] J.A. Dean, Lange's Handbook of Chemistry, English edition., Science Press, 2003, pp. 43–54 (Chapter 4).

[6] B.S. Kang, Y.W. Heo, L.C. Tien, D.P. Norton, F. Ren, B.P. Gila, S.J. Pearton, Hydrogen and ozone gas sensing using multiple ZnO nanorods, Applied Physics. **A 80** (2005) 1029–1032.

[7] B.S. Kang, F. Ren, Y.W. Heo, L.C. Tien, D.P. Norton, S.J. Pearton, pH measurements with single ZnO nanorods integrated with a microchannel, Applied Physics Letter **86** (2005) 112105–112107.

[8] H.T. Wang, B.S. Kang, F. Ren, L.C. Tien, P.W. Sadik, D.P. Norton, S.J. Pearton, J. Lin, Hydrogen-selective sensing at room temperature with ZnO nanorods, Applied Physics Letter **86** (2005) 243503–243505.

[9] T. Gao, T.H. Wang, Synthesis and properties of multipod-shaped ZnO nanorods for gas sensor applications, Applied Physics **A 80** (2005)1451–1454.

[10] Y. Dai, Y. Zhang, Q.K. Li, C.W. Nan, Synthesis and optical properties of tetrapod-like zinc oxide nanorods, Chem. Phys. Lett. **358** (2002) 83–86.

[11] J.Q. Xu, Y.P. Chen, D.Y. Chen, J.N. Shen, Hydrothermal synthesis and gas sensing characters of ZnO nanorods, Sensors and Actuators **B 113** (2006) 526–531.

[12] J.Q. Xu, Y.P. Chen, Y.D. Li, J.N. Shen, Gas sensing properties of ZnO nanorods prepared by hydrothermal method, Journal of Material Science **40** (2005) 2919–2921.

[13] F.F. Zhang, X.L.Wang, S.Y. Ai, Z.D. Sun, Q.Wan, Z.Q. Zhu, Y.Z. Xian, L.T. Jin, K. Yamamoto, Immobilization of uricase on ZnO nanorods for a reagentless uric acid biosensor, Anal. Chim. Acta **519** (2004) 155 – 160.

[15]Han Ho Choi, PhD Dissertation, Synthesis and characterization of tailoered zinc oxide nanostructures and their engineered nanocomposites, Florida State University, 2004.

[16] Silicon Far East, “EDX and WDX Analysis”, Available online: http://www.siliconfareast.com/edxwdx.htm. (Downloaded: 15 April 2007)

[17] Q. Y. Hlatshwayo, MSc Dessertation, Solid State Interaction Between Thin Metal Films and SiO_2 Substrates, University of Zululand, February 2000.

[18]Xing-Jiu Huang, Yang-Kyu Choi, Chemical sensors based on nanostructured materials, Sensors and Actuators **B 122** (2007) 659–671

[19] Guseong-dong, Yuseong-gu, Daejeon, South Korea, Institute of Science and Technology, 373-1

[20] N. Barsan, D. Koziej, U. Weimar, Metal oxide-based gas sensor research: How to?, Sensors and Actuators **B 121** (2007) 18-35

[21] P. Mitra, A.P. Chatterjee 1, H.S. Maiti ,ZnO thin film sensor, Materials Letters **35** (1998) 33-38

[22] K. Ip, G.T. Thaler, Hyucksoo Yang, Sang Youn Han,Yuanjie Li, D.P Norton S.J. Pearton, Soowhan Jang, F. Ren, Contacts to ZnO, Journal of Crystal Growth **287** (2006) 149-156

[23] Laudise R.A, Growth and perfection of crystals (in English), pages: 458-463

[24] Laudice R.A, Hydrothermal synthesis of Crystals, C&EN September 28:30-43

[25] B.H., Kang L., Nieh R., and Lee J.C., Applied physics Lett. **76, 1**926 (2000)

[26] Wikipedia, the free encyclopedia, “Rutherford Backscattering Spectroscopy”, Available online: http://en.wikipedia.org/wiki/Rutherford_Backscattering_Spectroscopy. (Downloaded:12 March 2007).

[27] Wikipedia, the free encyclopedia, “Pulsed Laser Deposition”, available online: http://en.wikipedia.org/wiki/Pulsed_laser_deposition. (Downloaded: 27 April 2008).

[28] Superconductivity Center at Argonne National Laboratory, “Pulsed Laser Deposition”, Available online: http://superconductivity.et.anl.gov/Techniques/images/PLD_schem.jpg. (Downloaded: 27 April 2008).

[29] Chemical Science Department, Kobe-u, “Hydrothermal Synthesis”,Available online: http://www.chem.sci.kobeu.ac.jp/~eda/image/research_3/hydrothermal_synthesis.jpg. (Downloaded: 27 April 2008).

[30] Zhitao Chen, Lian Gao, A facile route to ZnO nanorod arrays using wet chemical Method, Journal of Crystal growth **293** (2006) 522-527.

[31] Dewei Chu, Yu-Ping Zeng, Dongliang Jiang, Hydrothermal synthesis and optical properties of Pb^{2+} doped ZnO nanorods, Materials Letters **60** (2006) 2783-2785

[32] Paul A. Heiney, University of Pennsylvania, Physics Department, “X-ray Diffraction”, available online: http://www.physics.upenn.edu/~heiney/talks/hires/whatis.html. (Downloaded: 14 August 2008)

1 APPENDIX

1.1 One-Dimensional Metal oxide nanostructures.

One-dimensional metal oxide nanostructures such as nanorods, nanowires, and nanotubes are defined by their aspect ration, which is essentially the ratio of the outer diameter to their length.

Nanorods and Nanowires A literature survey of the synthesis and investigations of nanorods and nanowires of metal oxides, hydroxides, and oxyhydroxides is given below (sorted by alphabetic order of the chemical formula):

- Aluminium

α-Al_2O_3, γ-AlOOH, and γ-Al_2O_3

- Boron

$Al_{18}B_9O_{33}$ and MgB_4O_7

- Cadmium

CdO

- Cobalt

CoO and Co_3O_4

- Chromium

α-$Cr2O_3$ and $BaCrO_4$

- Copper

CuO, $Cu(OH)_2$, Cu2O, $GdBa_2Cu_3O_{6.5}$ and $YbaCu_3O_7$

- Europium

$Eu2O_3$

- Iron

α-FeOOH, β-FeOOH, α-Fe_2O_3 and Fe_3O_4

- Gallium

β-Ga_2O_3

- Indium

In_2O_3 and $SnIn_2O_3$

- Iridium

IrO_2

- Lanthanum

La $(OH)_3$

- Magnesium

MgO and Mg $(OH)_2$

- Manganese

γ-MnOOH, α-and β–MnO_2, δ-MnO_2, $LaBaMnO_3$, $LaCaMnO_3$, $LaSrMnO_3$ and Mn_3O_4

- Molybdenum

MoO_2 and –MoO_3

- Nickel

NiO and α–Ni $(OH)_2$

Lead PbO_2

- Ruthenium

RuO_2

- Antimony

Sb_2O_3, Sb_2O_4 and Sb_2O_5

- Silicon

SiO_2

- Tin

SnO_2

- Tantalum

$NaTaO_3$

- Titanium

TiO_2 and $BaTiO_3$

- Vanadium

VO_2, LiV_2O_4 and V_2O_5

- Tungsten

WO_x, WO_2, WO_3, $BaWO_4$ and $CdWO_4$

- Zinc

ZnO

- Zirconium

ZrO_2

***Table1**: Literature survey of orientated 3D arrays consisting of 1D metal oxide nanostructures (sorted alphabetically by the chemical formula and ascending diameter)*

***Adapted from**: Encyclopaedia of nanoscience and Nanotechnology, **Volume 8**: Pages (155-157)*

Material	**Morphology**	**Dimension(D*L)**	**Synthesis method**	**Ref**
Monoxide				
CdO	Nanowire	60nm * few μm	Alumina membrane	
CuO		30-100nm *15μm	Thermal oxidation	
Cu_2O		25-45nm *3-5μm 80-100nm * 10μm	Electrodeposition	
ZnO		15-40nm * 1μm	Molecular beam epitaxy	
	Nanorod	20nm*400nm	Pulsed laser deposition	
		25nm*800nm	Metallorganic vapour-phase epitaxy	
		45nm*200mn 70nm*600nm	Chemical vapour deposition	
		85-95nm*500nm	Epitaxial electrodeposition	
	Nanowire	55nm*2.6μm 190nm*15μm	Metal vapour deposition	
		90nm* 1μm	Electrodeposition in alumina membrane	
		150-250nm*2μm	Electrodeposition	
		100-200nm several μm in length	Aqueous chemical growth	
		10-200nm*2-20μm 20-120nm*5-20μm	Vapour-liquid-solid growth	

		15-90nm*few μm	Alumina membrane	
		200nm*50μm		
	Nanotube	150nm inner diam. 200nm outer diam. 60μm in length		
	Microtube	1μm inner diam. 2μm outer diam. 10μm in length	Aqueous chemical growth	
Dioxide				
CeO_2	Nanowire	100nm*1μm	Chemical vapour deposition	
$LiCoO_2$		100nm several μm in length	Alumina membrane	
$LiNi_{0}.5Co_{0.5}O_2$				
$LiNiO_2$		100nm*50μm		
$\propto$-MnO_2		200nm*50μm		
$LiMnO_2$		100nm*50μm		
$LiCo_{0.5}Mn0.5O2$	Nanorod	100nm*500nm		
PdO_2	Nanocone	40nm*500nm	Thermal oxidation	
		200nm*1.2μm		
SiO_2	Nanowire	50nm mm in length		
		125-200nm*10μm	Sol-gel electrophoresis in polycarbonate membrane	
	Nanoflower	20-120nm*10-250μm	Catalytic gas solid reaction	

	Nanotube	16-24nm inner diameter 30 nm outer diameter 6μm in length	Alumina membrane	
SnO_2	Nanorod	70nm several μm length		
TiO_2	Nanowire	10-40nm*2-10μm	Electrodeposition in alumina membrane	
		15nm*6 μm	Alumina membrane	
	Nanorod	40-50nm*140nm	Photoelectrochemical etching	
	Nanowire	125-200nm*10 μm	Sol-gel electrophoresis in the polycarbonate membrane	
		200nm*2 μm 500nm*8 μm	Magneton sputtering	
		15nm*30 μm	Alumina Membrane	
	Nanotube	2.5-5nm inner diameter 20-40nm outer diameter 0.3-0.9 μm in length		
		200nm outer diameter 50 μm in length		
		25-60 nm inner diameter 250nm in length	Anodic oxidation	

		50-70nm inner diameter 120nm outer diameter Several µm in length	Electrodeposition in the polymer coated alumina membrane	
ZrO_2		170-180nm inner diam. 200-233nm outer diam. 3 µm in length	Alumina membrane	
		170nm inner diameter 190nm outer diameter 50 µm in length		
		170nm inner diameter 280nm outer diameter several µm in length		
Trioxide				
MoO_3	Nanotube	20-150nm inner diameter 50-300nm outer diameter 5-8 µm in length	Chemical-vapour deposition	
WO_3	Nanowire	200nm*50 µm	Alumina membrane	
Sesquioxide				
Al_2O_3	Nanorod	5nm*860 nm 20-80nm*30-200 nm	Anodization	

	Nanotube	10-20nm inner diameter 40nm outer diameter 450 nm in length		
		12nm inner diameter 35nm outer diameter 650nm in length		
α-Fe_2O_3	Nanorod	2*500nm Bundles of 50nm	Aqueous chemical growth	
$In2O_3$	Nanowire	60 nm Several µm in length	Electrodeposition in the alumina membrane	
	Nanotube	100nm inner diameter 200nm outer diameter 50 µm in length	Alumina membrane	
β-Ga_2O_3	Nanowire	20-100nm*10-100 µm	Microwave plasma	
		60-150 nm Several µm in length	Chemical vapour deposition	
	Nanotube	100nm inner diameter 200nm outer diameter 50 µm in length	Alumina membrane	
Perovskite				
$BaTiO_3$	Nanowire	125-200nm*10 µm	Sol-gel electrophoresis in polycarbonate membrane	
$PbTiO_3$	Nanotube	200nm outer diameter 60 µm in length	Alumina membrane	
$PbZr_{0.52}Ti_{0.48}O_3$	Nanowire	125-200 nm *10 µm	Sol-gel electrophoresis in poly carbonate membrane	

Spinel oxide				
$LiMn_2O_4$	Nanotube	10nm inner diameter 200nm outer diameter several µm in length	Alumina membrane	
Co_3O_4	Nanowire	200nm*50 µm		
Pentoxide				
V_2O_5	Nanowire	300-600nm Several µm in length	Electrodeposition in polycarbonate membrane	
Miscellaneous				
β-FeOOH	Nanorod	5nm*500nm Bundles of 50nm	Aqueous chemical growth	
γ-MnOOH	Nanowire	100nm several µm in length		
$La0.7Sr0.2MnO_3$	Nanorod	100nm*500nm-1.5 µm	Pulsed laser deposition	
$La_{0.8}Sr_{0.2}MnO3$		25nm*70nm		
Sr_2Nb2O_7	Nanowire	125-200nm*10 µm	Sol-gel electrophoresis in poly carbonate membrane	
VO_4	Nanotube	5-50nm inner diameter 15-150 outer diameter 1-15 µm in length	Ligand-assisted template	
		15-45nm inner diameter 50-100 outer diameter 0.8-3µm in length		

		20-35nm inner diameter 70-140 outer diameter 2-12 µm in length		
WO_4	Nanorod	10-30nm*300nm	Electrochemical etching	
		10-30nm*500nm-1.6 µm	Thermal oxidation	